JGR Oceans

RESEARCH ARTICLE
10.1029/2024JC021754

Enhanced Passive Tracer Dispersion by an Energetic Internal Wave Continuum

C. P. Sanjay[1] and Jim Thomas[1,2]

[1]International Centre for Theoretical Sciences, Tata Institute of Fundamental Research, Bangalore, India, [2]Centre for Applicable Mathematics, Tata Institute of Fundamental Research, Bangalore, India

Key Points:

- We study passive tracer dispersion by flows composed of an internal wave continuum along with balanced eddies
- Increasing internal wave energy levels monotonically increases the forward cascade rate of tracer variance and steepens the tracer spectrum
- Our results emphasize the need to parameterize wave-induced effects on tracer dispersion in coarse resolution large-scale models

Correspondence to:
J. Thomas,
jimthomas.edu@gmail.com

Citation:
Sanjay, C. P., & Thomas, J. (2025). Enhanced passive tracer dispersion by an energetic internal wave continuum. *Journal of Geophysical Research: Oceans*, *130*, e2024JC021754. https://doi.org/10.1029/2024JC021754

Received 23 AUG 2024
Accepted 4 APR 2025

Abstract In this work we explore the impact of a broad spectrum of internal waves on the dispersion of passive tracers. We do so by looking at tracer dynamics in low Rossby number flows with different balance-to-wave energy levels generated by numerically integrating the Boussinesq equations. Our tracer dispersion experiments reveal that stirring, dispersion, and downscale cascading of tracers are enhanced on increasing wave energy level in the flow. Specifically, wave-dominated flows exhibit higher tracer spectral flux, steeper tracer variance spectra, and severe depletion of tracer variance across scales, compared to eddy-rich flows. Interestingly, our analysis also show that the dominant share of the tracer flux is located in regions of low vorticity values in eddy dominated flows and low horizontal divergence values in wave dominated flows. These findings point out that internal wave-induced effects on tracer dispersion cannot be neglected and needs to be accurately parameterized in large-scale models that do not directly resolve wave fields.

Plain Language Summary Oceans contain a major share of its kinetic energy in coherent structures known as eddies. These eddies are known to contribute significantly in the transport of tracers such as heat, salt, carbon, and other nutrients such as oxygen, nitrogen, etc. However, in recent times, in situ observations, satellite altimetry data, and global-scale model outputs have revealed that a broad spectrum of energetic internal waves coexist with the eddies in different oceanic regions. Inspired by these findings, in this work we numerically investigate wave-induced effects on tracer stirring and mixing in different flow regimes with varying wave-eddy energy ratios, while keeping the total flow energy the same across different regimes. We observe enhanced stirring and dispersion of tracers when wave energy content in the flow is increased. Notably, even a flow with similar wave and eddy energies exhibits about an order of magnitude increase in the downscale transfer and dissipation of tracers when compared to an eddy-dominated flow. Our results point out that internal waves can play an important role in oceanic tracer dispersion and emphasis the need to parameterize wave-induced effects in coarse resolution large-scale models.

1. Introduction

Oceanic flows play a major role in the transport, dispersion, and mixing of different kinds of tracers such as heat, salt, carbon, oxygen, and nitrogen (Booth & Kamenkovich, 2008; Gnanadesikan et al., 2013; McWilliams, 2008). At mesoscales, stirring of tracers along isopycnals or constant density surfaces is prominent (see for example J. Ledwell et al. (1993)). Large-scale models that do not completely resolve mesoscale stirring parameterizes its effects by setting the isopycnal diffusivity. Multiple studies have shown that isopycnal diffusivity is an important parameter that controls a broad set of oceanographic processes. For instance, Gnanadesikan et al. (2015) showed that isopycnal diffusivity values set in models can significantly affect the oceans' uptake of anthropogenic carbon, which in turn can affect global warming. Chouksey et al. (2022) used ocean models to show that an increase in isopycnal diffusivity value can weaken both Atlantic residual overturning circulation as well as Antarctic circumpolar current. Additionally, Holmes et al. (2022) looked at the sensitivity of a global ocean model on the variability of isopycnal diffusivity and showed that the magnitude and spatial structure of isopycnal diffusivity can significantly affect the tracer structure as well as ocean circulation. Another study by C. Jones and Abernathey (2019) also pointed out that the variations in isopycnal diffusivity can control ocean ventilation by influencing the pathway along which water reaches the deep Pacific. These studies in turn emphasis the need to better understand and capture lateral stirring processes accurately in ocean models.

While balanced eddy dynamics are significant at large mesoscales (∼100 km), submesoscales (<10 km) are energized by internal waves, because the waves forward cascade their energy from large forcing scales to smaller

scales. Dispersion of tracers at such small-scales is primarily due to breaking internal gravity waves (Whalen & Coauthors, 2020; Kunze, 2017; Naveira Garabato et al., 2004; J. R. Ledwell et al., 2011; Gregg et al., 2003; Waterhouse et al., 2014; N. Jones et al., 2020; Katsumata et al., 2021; Whitwell et al., 2024). We therefore have a paradigm where large-scale stirring is primarily considered to be due to mesoscale eddies while small-scale tracer dispersion is attributed to internal wave breaking and mixing events. As a result, small-scale diapycnal diffusivity is set based on wave energy levels and wave breaking parameters.

Since balanced eddies arise as a result of turbulent cascades in the quasi-geostrophic (QG) turbulence based in the small Rossby number regime, it is a usual practice to compare the results of tracer dispersion studies with tracer predictions resulting from the QG model. Specifically, for passive tracers that are advected by the flow, such as spice in the ocean, the flow spectra arising from QG theory can be used to predict the tracer variance spectra (Vallis, 2006). Intriguingly, such comparisons have often led to unexpected departures from QG predictions. For example, Klymak et al. (2015) observed that in the Gulf of Alaska, tracer variance spectra showed considerable deviations from the predictions of QG theory at submesoscales. By analyzing spice distributions in the Bay of Bengal, Spiro Jaeger et al. (2020) reported that tracer variance spectrum was steeper than that predicted by QG theory at scales less than 10 km. Further disagreements were also observed in the spectrum of salinity anomalies from the Sargasso Sea (Kunze et al., 2015). On a different route, tracer release experiments conducted in the North Atlantic also obtained a similar result: dispersion of tracers at the scale of 1–10 km was found to be much higher than the analytical predictions based on simple theories (J. R. Ledwell et al., 1998). Similarly, measurements from dye patterns in the New England shelf (M. Sundermeyer & Ledwell, 2001; M. A. Sundermeyer & Lelong, 2005) and studies examining the upper ocean thermohaline structure (Cole et al., 2010; Cole & Rudnick, 2012; Ferrari & Rudnick, 2000) found that lateral dispersion and stirring of tracers at submesoscales are more efficient than that expected based on QG predictions.

Oceanic flows, although dominated by balanced eddy rich flows, also contain different kinds of internal gravity waves. In general, balanced flows or eddy-rich flows, tend to be more two-dimensional in nature and are often characterized by smooth large-scale gradients with little vertical motion. On the other hand unbalanced wave-rich flows behave more like fully three-dimensional flows with significant vertical variability. Interestingly, over the past two decades a broad set of datasets from satellite altimeter, in situ measurements, and global-scale simulations have reinstated the presence of an energetic broad spectrum of internal waves alongside the balanced flow in different regions of the oceans (Lien & Sanford, 2019; Pinkel, 2014; Qiu et al., 2017, 2018, 2022; Richman et al., 2012; Savage & Coauthors, 2017; Tchilibou et al., 2018; Torres et al., 2018; Vladoiu et al., 2024; Yu et al., 2019). These studies specifically point out that internal gravity wave energy levels increase as we move towards smaller spatial scales, with multiple oceanic regions having dominant share of their flow energy in internal waves at submesoscales.

Inspired by above mentioned observations, theoretical, numerical, and observational studies looking at interactions between waves and balanced flows have found that internal waves can exchange energy with and modify balanced flow dynamics in different parameter regimes (see energy exchange results detailed in Thomas (2023)). At this point there is an improved understanding of different kinds of wave-balance energy exchanges and how these interactions affect balanced flow energy changes. However, the effect that internal waves have on tracer dispersion remains unclear, despite several previous observational studies, realistic ocean model based studies, and idealized studies using reduced mathematical models in two dimensions and three dimensions hinting that the presence of internal waves could modify tracer dispersion features (Hernandez-Duenas et al., 2021; Meyerjurgens et al., 2020; Suanda et al., 2018; Thomas & Gupta, 2022).

Multiple observational studies mentioned above that found enhanced tracer stirring at submesoscales speculated the possibility of unbalanced flows, in the form of internal waves, being an ingredient that contributed to enhanced tracer dispersion. Consequently, in this work, we numerically integrate the Boussinesq equations to construct flow regimes having different wave-balance energy levels and advect tracer fields to explore how its dispersion is affected by internal waves. We specifically consider a broad spectrum of waves forming an internal wave continuum and study its effect on tracer dispersion. The plan for the paper is as follows: Section 2 presents the governing equations and the different flow regimes, tracer dispersion results in the different regimes is presented in section 3, and we summarize our findings in section 4.

2. Equations and the Flow Regimes

The turbulent flows for this study were obtained by numerically integrating the Boussinesq equations, which in non-dimensional form are:

$$\frac{\partial \mathbf{v}}{\partial t} + \hat{\mathbf{z}} \times \mathbf{v} + \nabla p + Ro\left(\mathbf{v} \cdot \nabla \mathbf{v} + w \frac{\partial \mathbf{v}}{\partial z}\right) = \mathbf{F}_v - \nu \Delta^8 \mathbf{v} \tag{1a}$$

$$\frac{\partial w}{\partial t} + \alpha^2 \left(\frac{\partial p}{\partial z} - b\right) + Ro\left(\mathbf{v} \cdot \nabla w + w \frac{\partial w}{\partial z}\right) = F_w - \nu \Delta^8 w \tag{1b}$$

$$\frac{\partial b}{\partial t} + w + Ro\left(\mathbf{v} \cdot \nabla b + w \frac{\partial b}{\partial z}\right) = F_b - \nu \Delta^8 b \tag{1c}$$

$$\nabla \cdot \mathbf{v} + \frac{\partial w}{\partial z} = 0 \tag{1d}$$

where $\mathbf{v} = (u, v)$ is the horizontal velocity vector, w is the vertical velocity, p is the pressure, b is the buoyancy, and $\hat{\mathbf{z}}$ is the unit vector along the vertical direction. To obtain the above equations from the dimensional Boussinesq equations, we non-dimensionalized velocity by a velocity scale U^*, horizontal spatial coordinates by a length scale L^*, vertical coordinate by a length scale H^*, and time by the inverse of inertial frequency, $1/f^*$, where we use '*' to denote dimensional variables. The continuity equation was then used to obtain the scale for vertical velocity as U^*H^*/L^*, geostrophic balance was used to obtain the scale for pressure as $f^*U^*L^*$, and hydrostatic balance was used to obtain the scale for buoyancy as $f^*U^*L^*/H^*$. Non-dimensionalizing the equations using these variables gives us Equation 1 with Rossby number $Ro = U^*/f^*L^*$ and $\alpha = N^*/f^*$, where N^* is the buoyancy frequency.

Oceanic measurements have shown that the buoyancy frequency, N^*, can vary both geographically and seasonally between 10^{-3} s^{-1} $-$ 10^{-2} s^{-1} (Emery et al., 1984; Li et al., 2020; Lien & Sanford, 2019; Sallée et al., 2021). By considering $f^* \sim 10^{-4}$ s^{-1} we can see that in the oceans α can vary between $10-100$. In our simulations we set $\alpha = 20$, which is in the above-mentioned range. Furthermore, in this study we will be based in the small Rossby number regime and chose $Ro = 0.1$.

The variables $\mathbf{F}_v$, F_w, and F_b in Equation 1 denote forcing on the flow fields $\mathbf{v}$, w, and b, respectively. $\nabla = (\partial/\partial x, \partial/\partial y)$ is the horizontal gradient operator while $\Delta = \nabla^2 + \partial^2/\partial z^2$ is the three dimensional Laplacian operator. We used hyperdissipation operators $\nu\Delta^8$ on the flow variables above to restrict dissipation to grid scales and thereby obtain a broad range of inviscid scales in the inertial range. In the absence of forcing and dissipation, Equation 1 conserves energy, given by the following equation:

$$\frac{\mathrm{d}E}{\mathrm{d}t} = 0 \; ; \; E = \frac{1}{2}\int_{\mathcal{D}} \left(\mathbf{v}^2 + \frac{w^2}{\alpha^2} + b^2\right) \mathrm{d}\mathbf{x} \, \mathrm{d}z \tag{2}$$

where $\mathbf{x} = (x, y)$ and the integration is performed over the entire domain $\mathcal{D}$.

Setting $Ro = 0$ in Equation 1 and temporarily ignoring the forcing and dissipation terms allow us to decompose the flow fields into wave and balance components as follows:

$$\frac{\partial \mathbf{v}_W}{\partial t} + \hat{z} \times \mathbf{v}_W + \nabla p_W = 0 \tag{3a}$$

$$\frac{\partial w_W}{\partial t} + \alpha^2 \left(\frac{\partial p_W}{\partial z} - b_W\right) = 0 \tag{3b}$$

$$\frac{\partial b_W}{\partial t} + w_W = 0 \tag{3c}$$

$$\nabla \cdot \mathbf{v}_W + \frac{\partial w_W}{\partial z} = 0 \tag{3d}$$

$$\hat{z} \times \mathbf{v}_G + \nabla p_G = 0 \tag{4a}$$

$$\frac{\partial p_G}{\partial z} - b_G = 0 \tag{4b}$$

$$w_G = 0 \tag{4c}$$

$$\nabla \cdot \mathbf{v}_G = 0 \tag{4d}$$

The subscripts "W" and "G" in the above equations are used to represent internal waves and geostrophic balanced component, respectively. Notably, the above decomposition provides us with linear internal gravity waves in the flow that is orthogonal to the balanced field such that the total energy of the flow is obtained as the sum of energies of the components, that is, $E = E_G + E_W$. For internal waves, the dispersion relation connecting frequency of waves with the horizontal and vertical wavenumbers obtained from above wave equations is given by the following equation:

$$\omega^2 = \frac{k_h^2 + k_z^2}{k_h^2/\alpha^2 + k_z^2} \tag{5}$$

where ω is the frequency, $k_h = \sqrt{k_x^2 + k_y^2}$ is the horizontal wavenumber with k_x and k_y as the wavenumbers in the x and y directions, respectively, and k_z is the vertical wavenumber. Equation 5 in dimensional form reads as $\omega^{*2} = \left(N^{*2}k_h^{*2} + f^{*2}k_z^{*2}\right)/\left(k_h^{*2} + k_z^{*2}\right)$, this being the well-known internal gravity wave dispersion relationship stemming from non-hydrostatic linear Boussinesq equations (Vallis, 2006).

It is important to note that the decomposition given in Equations 3 and 4 used the linear equations. In the nonlinear equations, it is a priori unclear if the unbalanced motions are pure linear waves that follow abovementioned dispersion relationship. To maintain this difference in our terminology, despite being based in the low Rossby number regime, we will call the unbalanced part of the flow as ageostrophic component and denote the fields with subscript "AG." We computed these fields as $u_{AG} = u - u_G$, $v_{AG} = v - v_G$ and so on. In the limit $Ro = 0$, the ageostrophic component will be pure linear waves.

As mentioned earlier, our goal is to examine the effect of waves and balanced flows on tracer dispersion in an idealized setting, ignoring all other external agencies, such as the presence of boundaries for example. To generate flows, we therefore numerically integrated Equation 1 in a domain $(\mathbf{x}, z) \in [0, 2\pi]^3$ with periodic boundary conditions in all the three directions using a de-aliased pseudo-spectral method. We used periodic boundary conditions keeping in mind that our goal is to understand small-scale dynamics where internal wave effects are important, and also to remove any boundary related effects from our study. In each direction we chose 384 grid points, which was sufficient to obtain a well-defined inertial range for both the flow and tracer field. Selected experiments were performed with higher resolutions, such as 512^3, to ensure that the results we describe below were not sensitive to the numerical resolution and that the resolution of 384^3 was sufficient to resolve the turbulent dynamics associated with the flow and the tracer field.

We evolved the flow as well as the tracer field using RK4 time stepping scheme with time step $\delta t = 0.01$. Based on multiple iterative simulations at a spatial resolution of 384^3, we chose $\nu = 10^{-34}$ as the flow diffusivity. At $t = 0$, internal waves and the balanced flow fields were introduced at low wavenumbers, $k_h \leq 5$ and $k_z \leq 5$. A stochastic forcing scheme was used to force the ageostrophic and balanced components separately at the low wavenumbers, $k_h \leq 5$ and $k_z \leq 5$, to attain desired balanced and unbalanced energy levels. The forcing generated higher wavenumbers and frequencies in the internal wave field, leading to the formation of an internal wave continuum. All the results presented in this work were obtained during the forced-dissipative equilibrium state. We refer the reader to Appendix A for more details about the stochastic flow forcing scheme.

Numerical integrations of Equation 1 were used to generate flows in three different regimes: QG regime where $E_G/E_{AG} \gg 1$, comparable wave (CW) regime where $E_G/E_{AG} \approx 1$, and strong wave (SW) regime where $E_G/E_{AG} \sim \mathcal{O}(Ro^2)$. As can be shown by asymptotic analysis (Thomas, 2023) and numerical integrations (Thomas

Table 1
Table Shows the Effective Rossby Number (Ro_{eff}), Time-Averaged Values of Total Energy ($\bar{E}$), Balanced Energy ($\bar{E}_G$), Ageostrophic Energy ($\bar{E}_{AG}$), Balance-to-Ageostrophic Energy Ratio ($\bar{E}_G/\bar{E}_{AG}$), the Relaxation Term Coefficient (γ), Time-Averaged Domain-Integrated Tracer Variance ($\overline{\Theta}$), and Tracer Cascade Efficiency ($\tilde{\eta}$)

Case	Ro_{eff}	$\bar{E}$	$\bar{E}_G$	$\bar{E}_{AG}$	$\bar{E}_G/\bar{E}_{AG}$	γ	$\overline{\Theta}\,(\times 10^{-4})$	$\tilde{\eta}$
QG	0.021	5.990	5.989	0.001	5.989×10^3	75	1.570	0.003
CW	0.084	6.020	3.010	3.010	1.000	3	1.590	0.060
SW	0.080	6.060	0.069	5.999	0.011	0	1.560	0.080

& Daniel, 2021), the effect of waves on balanced flow is asymptotically weak in the CW regime, while in the SW regime waves can severely impact balanced flow dynamics and inhibit coherent vortex formation. The flow regimes we obtain here are similar to those generated in Thomas and Daniel (2021) with one difference: Thomas and Daniel used freely evolving flows while we generate forced-dissipated flows with fixed energy levels. In all the regimes we maintained the total flow energy, $E \approx 6$, an O (1) value, while varying the relative amount of ageostrophic and balanced energy. In the QG regime the forcing acted only on the balanced component, while in the CW and SW regimes both wave and balanced flow fields were forced to maintain the required energy levels. While wave forcing strength was similar in both regimes, balanced forcing had to be much stronger in the SW regime due to much higher balanced energy dissipation in the SW regime. Below we will examine how energetic waves of O (1) amplitude impact tracer stirring and dispersion in both CW and SW regime.

Recall that we set $Ro = 0.1$ in Equation 1 to generate flows that are weakly nonlinear with asymptotically small Rossby numbers. A more precise integral estimate for the flow Rossby number may be obtained by calculating the domain and time-averaged Rossby number, which we will identify as the effective Rossby number, Ro_{eff}. We define this parameter using dimensional variables as $Ro_{\text{eff}} = \zeta^*_{\text{rms}}/f^*$, where ζ^*_{rms} is the dimensional time-averaged root-mean-square vertical vorticity. Using the non-dimensionalization procedure discussed below Equation 1, we write $\zeta^*_{\text{rms}} = \left(U^*\zeta_{\text{rms}}\right)/(L^*)$ such that ζ_{rms} is the dimensionless time-averaged root-mean-square value of the vertical component of the vorticity. This allows us to write $Ro_{\text{eff}} = \left(U^*\zeta_{\text{rms}}\right)/(L^*f^*) = Ro\zeta_{\text{rms}}$. The values of Ro_{eff} obtained for each of the regimes are listed in the second column of Table 1. Notice that this is an asymptotically small parameter, that is, $Ro_{\text{eff}} \ll 1$, confirming that the flow is weakly nonlinear and will have linear waves. The other columns in Table 1 show the time-averaged energy of the total flow, balanced flow, ageostrophic flow, and their ratio. Notice that the QG regime has negligible ageostrophic energy while the SW flow has 1% of its energy associated with the balanced flow.

The left column of Figure 1 shows the snapshots in time of the flow structures, with the plotted field being geostrophic vorticity, $\zeta_G = \hat{\mathbf{z}} \cdot \nabla \times \mathbf{v}_G$, in the QG and CW regimes and horizontal divergence, $\nabla \cdot \mathbf{v}$, in the SW regime. To highlight interior dynamics, in these figures we show the bottom half of the domain where the top facing plane is $z = \pi$ and $z = 2\pi$ plane becomes the bottom surface. The right column of the figure shows the flow energy spectra and its decomposition into geostrophic and ageostrophic energy spectra. In panel (a) we see the QG flow being composed of large and small coherent vortices along with fine scale vorticity filaments. The corresponding energy spectra in panel (b) shows that the total flow spectrum (black curve) overlaps with the balanced spectrum (blue curve) because the ageostrophic spectrum (red curve) is several orders of magnitude below. We also see that the geostrophic spectrum closely follows a -3 slope line. The CW regime shown in panel (c) is composed of coherent vortices and small-scale structures formed as result of wave interactions. The spectra in panel (d) shows that the balanced flow follows a slope of -3, whereas the ageostrophic spectra closely follows $-5/3$ slope. Finally, panel (e) shows the horizontal divergence since the balanced flow is extremely weak in this flow, as seen in panel (f) showing the blue balanced spectrum being several orders of magnitude below the red ageostrophic spectra. The SW regime is therefore the exact opposite of the QG regime, with the flow being composed almost entirely of the ageostrophic flow.

The three flow fields described above have almost the same total energy level, as seen in the third column of Table 1, while the unbalanced flow component's energy increases as we go from QG to SW. As a result, the flow dynamics of these three flows are very different. Below we will compare how the three different flows stir and disperse tracer fields.

3. Tracer Dispersion in Different Flow Regimes

Once turbulent flows in forced-dissipative equilibrium with specified energy levels were set up, we advected a passive tracer field θ by integrating the following equation:

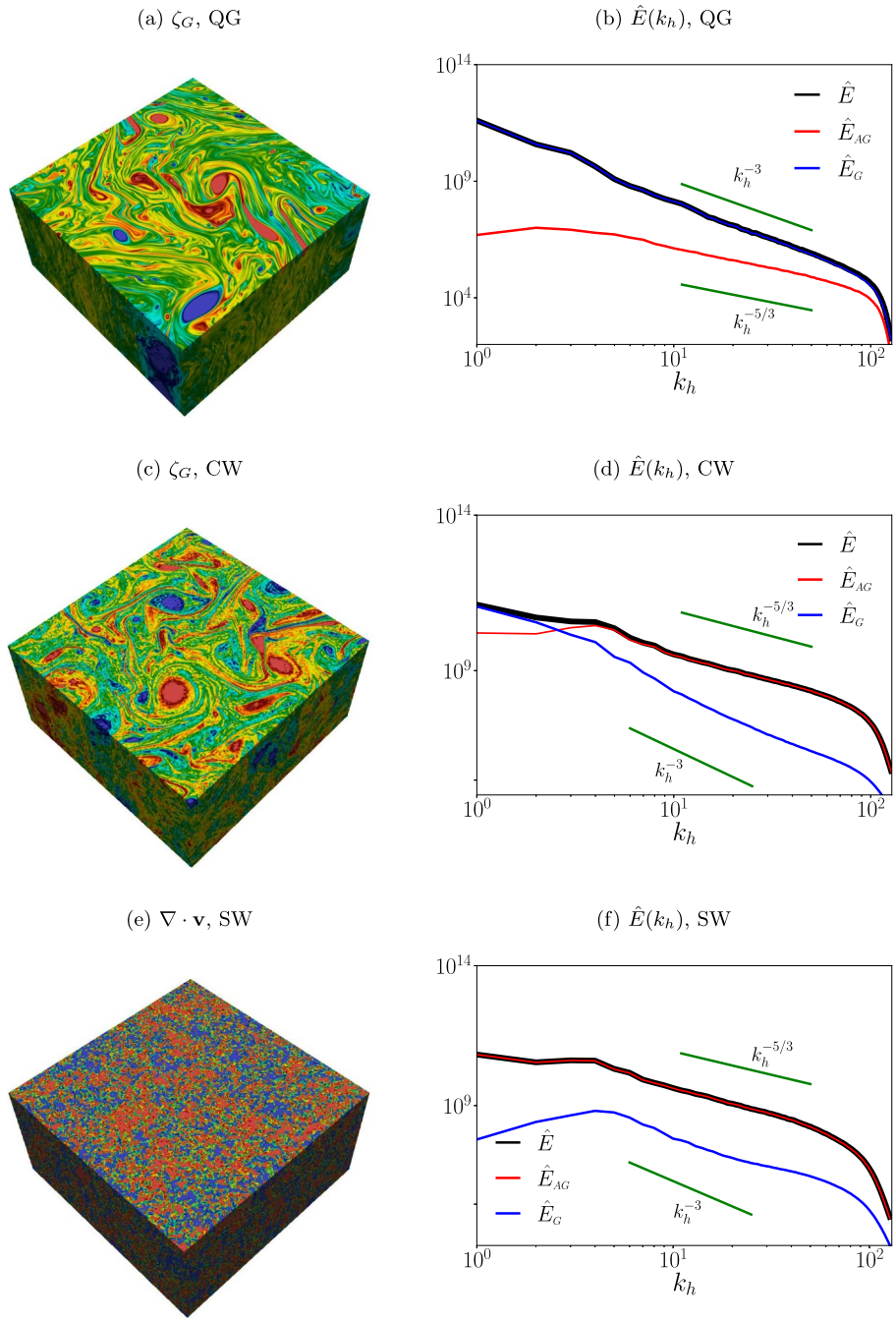

Figure 1. Snapshots of geostrophic vorticity in quasi-geostrophic (QG) (a) and comparable wave (CW) (c) regimes along with the horizontal divergence in strong wave (SW) regime (e) are shown in the left column. To emphasize the flow features within the interior, the panels above display bottom half of the domain, with the top surface at $z = \pi$ and the bottom surface at $z = 2\pi$. The horizontal energy spectra in QG (b), CW (d), and SW (f) regimes are shown above in the right column. The horizontal energy spectra are further split into balanced and ageostrophic components. Lines with slope −5/3 and −3 are included for comparisons.

$$\frac{\partial \theta}{\partial t} + (\mathbf{v} \cdot \nabla)\theta + w\frac{\partial \theta}{\partial z} = F_\theta - \gamma\theta - \nu_\theta \Delta^8 \theta \tag{6}$$

where F_θ represents tracer forcing, $\gamma\theta$ is a relaxation term, and $\nu_\theta\Delta^8\theta$ represents the hyperdissipation term. In the absence of forcing and dissipation, Equation 6 satisfies the conservation of tracer variance integrated over the domain as follows:

$$\frac{d\Theta}{dt} = 0,\ \Theta(t) = \frac{1}{2}\int_D \theta^2\ \mathrm{d}\mathbf{x}\ \mathrm{d}z. \tag{7}$$

Hereafter we will use tracer variance to denote pointwise tracer field squared, that is, θ^2, and refer to Θ as domain-integrated or net tracer variance.

The tracer dissipation term in Equation 6 removes tracer variance cascading and reaching grid scale, thereby avoiding tracer variance accumulation at the smallest scales. We set the tracer hyperdiffusivity $\nu_\theta = 10^{-32}$ to ensure tracer dissipation at the smallest possible scale in the domain such that an inertial range spanning almost a decade of wavenumbers is obtained. We forced the tracer by maintaining the initial tracer variance at the domain scale, $k = 1$, to generate tracers fields with the same net tracer variance in all three flow regimes. However, forcing alone was seen to be insufficient to maintain the same net tracer variance in all regimes; for instance, the tracer field in the QG regime was seen to equilibrate at a different net tracer variance than the tracer in the SW flow. Consequently, we used the relaxation term $\gamma\theta$ in Equation 6 to achieve the same net tracer variance in all cases. Notably, γ acted only on $k = 1$ wavenumber, similar to the forcing, thereby ensuring that the inertial range was unaffected by the forcing and relaxation terms. For the QG and CW regimes we used $\gamma = 75$ and $\gamma = 3$, respectively, to equilibrate tracer variance at the same level as in the SW regime, where we set $\gamma = 0$. Thus, we attained almost similar values of net tracer variance in all the flow regimes at equilibrium. The time-averaged net tracer variance values $(\overline{\Theta})$ are listed in the second to last column of Table 1 for comparison.

In addition to the above mentioned set up where we forced and maintained net tracer variance in all three flow regimes, we explored two other tracer set ups: (a) freely evolving tracer fields, where tracer fields reached no equilibrium, and (b) constant tracer variance injection case, where the tracer fields equilibrated at different domain-integrated values in the different flows. The results from these experiments were qualitatively similar to those found in experiments where we maintained net tracer variance and these two cases are discussed in appendix B. In the reminder of this section we will describe in detail the results from the specific set up where we maintained the same net tracer variance across all flow regimes.

In the left column of Figure 2 we show the tracer physical structure in the three regimes. Similar to Figure 1, for the tracers also we show the lower half of the domain with $z = \pi$ being the top plane. In panel (a) showing the tracer field in the QG regime, we see that stirring of the tracer is due to small scale vortices and vorticity filaments seen in Figure 1a, while the tracer is homogenized in bigger vortices. In contrast, panels (c) and (e) of Figure 2 shows much more dispersion of the tracer in the CW and SW regimes, respectively. The right column of Figure 2 shows the tracer variance spectra along horizontal, vertical, and total wavenumbers. The horizontal tracer spectra were computed by obtaining the tracer variance spectra along each z plane and then performing a summation over all the z planes. The vertical spectra in panel (d) was obtained by computing the tracer spectra along the vertical wavenumber k_z for each horizontal point $\boldsymbol{x}$ and then summing the spectra over all $\boldsymbol{x}$. The total spectra in panel (f) was obtained by taking the three-dimensional Fourier transform of the tracer field and then computing the tracer variance as a function of the three-dimensional wavenumber $k = \sqrt{k_h^2 + k_z^2}$. From panel (b), for the CW and SW cases we see a sharp drop in tracer variance at low wavenumbers followed by relatively low values of tracer variance in the inertial range, while the QG case shows a gradual drop in variance across scales. Similar qualitative feature is seen for tracer variance along vertical and total wavenumbers shown in panels (d) and (f). Flows that stir and cascade tracer variance downscale more efficiently will deplete more tracer variance from the inertial range. Consequently, the more pronounced depletion of the tracer variance in the CW and SW regime when compared to the QG regime is an indication of enhanced tracer stirring by the unbalanced flow components. We further notice that the drop in tracer variance from low horizontal wavenumbers is more pronounced for the SW regime when compared to the CW regime, hinting that the SW flow is more efficient than the CW flow in dispersing and downscale cascading of tracers. In summary, the right column of Figure 2 indicates that tracer stirring is enhanced both in the lateral as well as vertical directions in flows that contain internal waves.

To quantify the downscale cascade rate of tracer fields we now will examine the spectral flux of the tracer variance along total, horizontal, and vertical wavenumbers. For the flux along total wavenumbers, we performed a three-dimensional Fourier transform of Equation 6, temporarily dropping all the forcing and dissipation terms on the right hand side, to obtain the following equation:

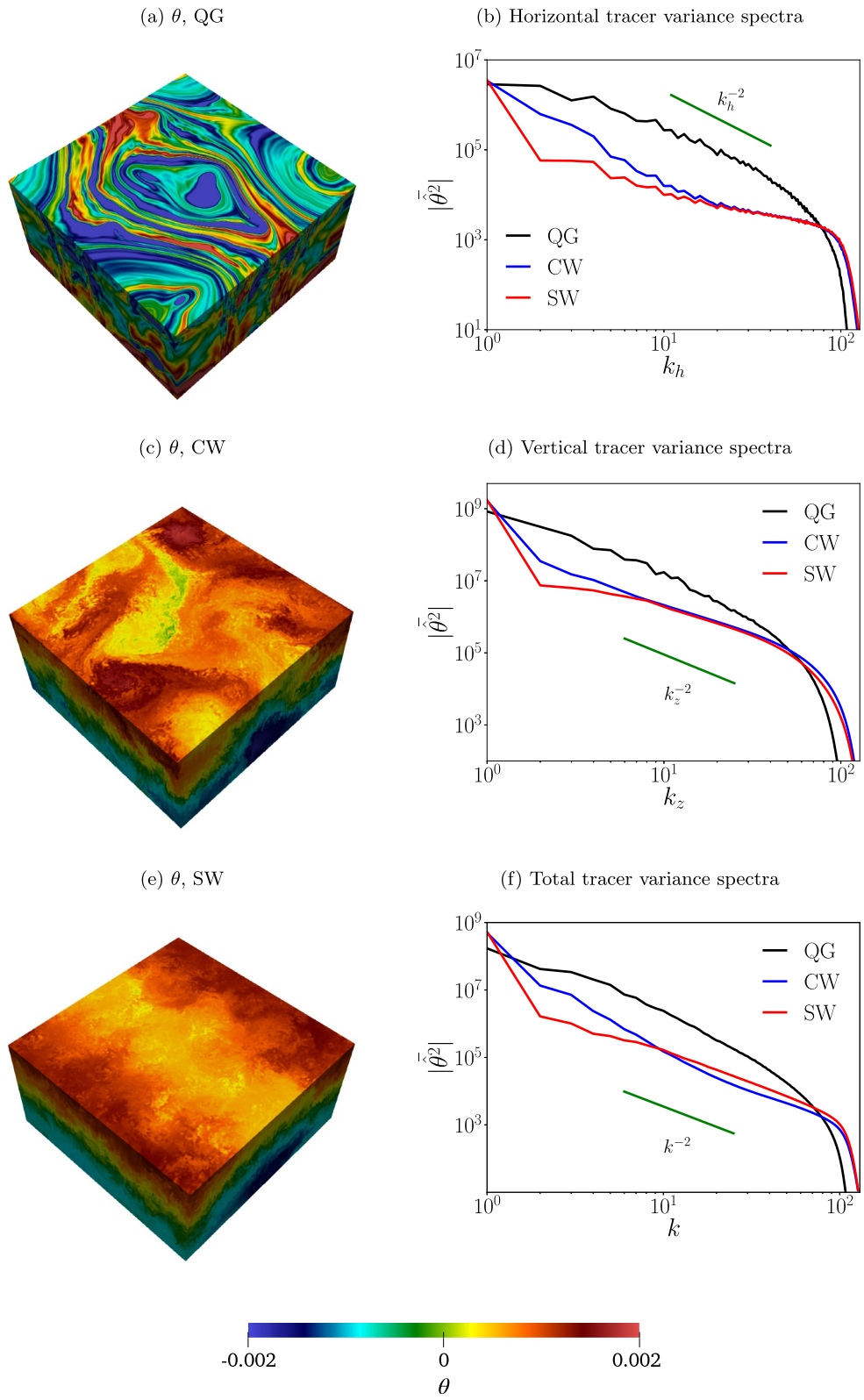

Figure 2. Left column shows tracer structures corresponding to the flows shown in Figure 1. Right column shows time-averaged horizontal, vertical, and total tracer variance spectra in the three regimes. Lines with slope −2 are included for reference.

$$\frac{\partial \hat{\theta}}{\partial t} + \nabla \cdot \widehat{(\theta \mathbf{v})} + \frac{\partial \widehat{(\theta w)}}{\partial z} = 0 \tag{8}$$

where the over-hat is used to represent the field quantities in Fourier space. Multiplying Equation 8 by the complex conjugate of $\hat{\theta}$ and adding to that equation the complex conjugate of the same equation gives us the time evolution of tracer variance contained at a specific wavenumber. Summing that equation over the band of wavenumbers $[k, k_{\max}]$ gives us the following equation:

$$\frac{\mathrm{d}}{\mathrm{d}t} \sum_{q=k_{\max}}^{k} |\hat{\theta}(q,t)|^2 = \hat{\Pi}(k,t). \tag{9}$$

The left hand side of Equation 9 denotes the rate of change of tracer variance in the band of wavenumbers $[k, k_{\max}]$ and $\hat{\Pi}(k,t)$ is the tracer variance flux, indicating the rate of transfer of tracer variance into or from the band of wavenumbers $[k, k_{\max}]$. A positive value of $\hat{\Pi}$ denotes a downscale cascade (into the wavenumber band, $[k, k_{\max}]$), while a negative value denotes an upscale cascade (from the wavenumber band, $[k, k_{\max}]$). We also performed a time averaging of $\hat{\Pi}(k,t)$ to obtain net averaged tracer flux along k which is denoted as $\overline{\hat{\Pi}}$.

Along the same lines as above, we calculated lateral or horizontal and vertical fluxes separately. To compute the horizontal tracer flux, we first obtained an equation similar to Equation 8 by performing a two dimensional Fourier transform of Equation 6 on each z plane and then followed similar manipulations as above to get a tracer flux equation on each z-plane as follows:

$$\frac{\mathrm{d}}{\mathrm{d}t} \sum_{q=k_{hmax}}^{k_h} |\hat{\theta}(q,z,t)|^2 = \hat{\Pi}_h(k_h,z,t). \tag{10}$$

The right hand side of above equation is the horizontal tracer variance flux that indicates the rate of tracer variance transfer at a particular horizontal wavenumber k_h on a fixed z-plane. Summing the above equation over all z and time-averaging the right hand side gives us the net averaged tracer flux along k_h, which we denote as $\overline{\hat{\Pi}}_h$.

For the vertical tracer flux, we performed a Fourier transform of the tracer equation along z for a fixed $\boldsymbol{x}$ and followed similar manipulations as above to get the following equation:

$$\frac{\mathrm{d}}{\mathrm{d}t} \sum_{q=k_{zmax}}^{k_z} |\hat{\theta}(\mathbf{x},q,t)|^2 = \hat{\Pi}_z(\mathbf{x},k_z,t). \tag{11}$$

where the above equation applies for fixed horizontal point $\mathbf{x}$. Summing above equation over all $\mathbf{x}$ and time-averaging, the right hand side gives us the averaged vertical tracer flux $\overline{\hat{\Pi}}_z$.

From the above discussions it is noted that the computation of total flux $(\hat{\Pi})$ involved a three-dimensional Fourier transform of Equation 6. To compute the horizontal flux $(\hat{\Pi}_h)$ we performed a two dimensional Fourier transform followed by an integration along the vertical direction. The vertical flux $(\hat{\Pi}_z)$ is obtained after a one dimensional transform and then performing integrations along the horizontal directions. From the flux calculation procedures, notice that the three fluxes—horizontal, vertical, and total—mean different things and cannot be compared with each other. Additionally, it is important to note that the total flux cannot be expressed as the sum of horizontal and vertical fluxes.

The left column of Figure 3 shows the total, horizontal, and vertical tracer fluxes in the three flow regimes. We see that the QG flow is associated with the lowest flux, SW the highest, and the CW flow leading to a flux that lies close to the SW case, much higher than QG. Notably, the fluxes in SW and CW is almost an order of magnitude higher than that in the QG case. We also see that the total flux and the horizontal flux, shown in panels (a) and (c) have a well-defined inertial range with constant flux, while the vertical flux, shown in panel (e), did not generate a constant flux inertial range even after long time-averaging of the flux. It is possible that getting a clear inertial

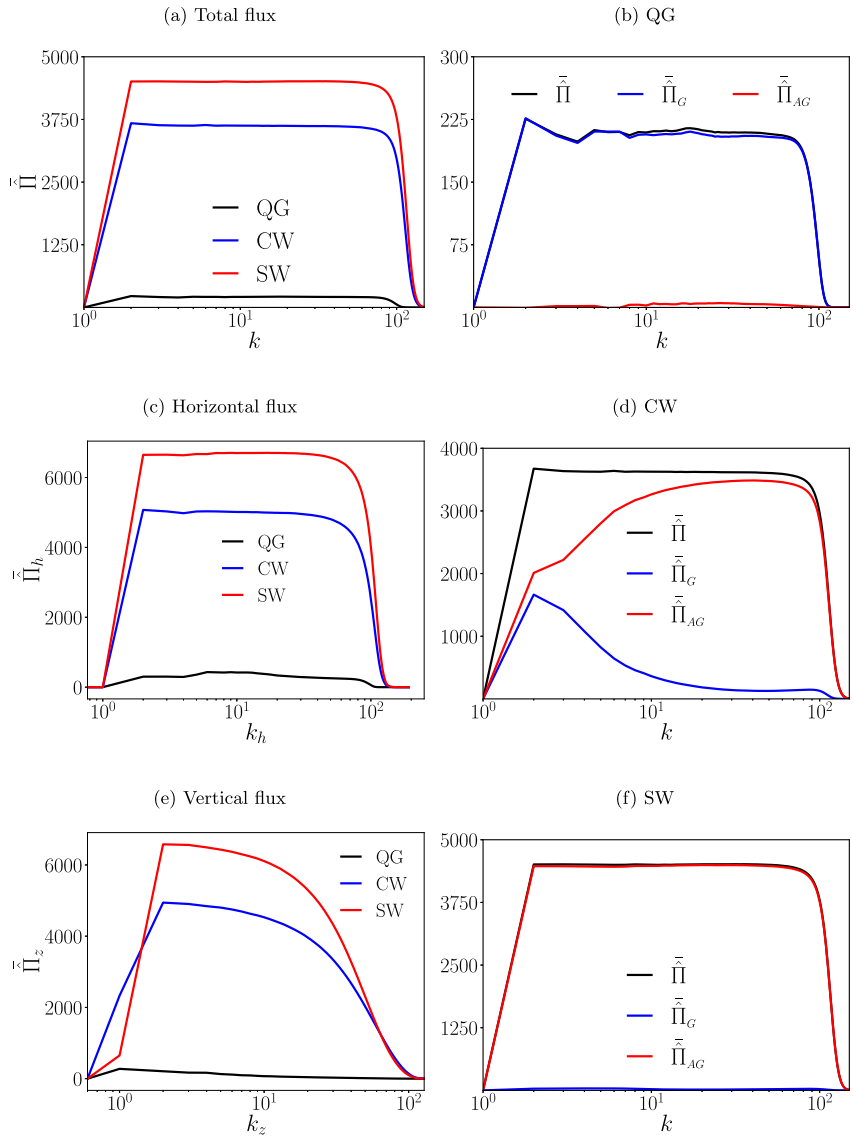

Figure 3. Time-averaged total (a), horizontal (c), and vertical (e) tracer variance flux for the three flow regimes. The total tracer variance flux is further split into geostrophic and ageostrophic parts in QG (b), CW (d), and SW (f) regimes. In panel (f) the red line completely overlaps with the black curve indicating the dominance of ageostrophic component in determining the downscale transfer flux.

range in vertical flux requires much higher resolution than the ones we used. Nevertheless, the comparison of the fluxes in the different regimes indicate that the presence of internal wave containing ageostrophic flow can lead to a much higher downscale cascading rate of the tracer field in both lateral and vertical directions. To further substantiate this finding, we decomposed the different fluxes into contributions from geostrophic and ageostrophic flow components.

We applied the decomposition in Equations 3 and 4 to split the velocity fields as $\mathbf{v} = \mathbf{v}_G + \mathbf{v}_{AG}$, $w = w_G + w_{AG}$. We then used these velocity components in Equation 8 and obtained Equation 9 such that the flux is decomposed into balanced and ageostrophic contributions as $\hat{\Pi} = \hat{\Pi}_G + \hat{\Pi}_{AG}$. The right column of Figure 3 shows the total flux in the three flow regimes and their decomposition into geostrophic and ageostrophic components. For the QG regime shown in Figure 3b, we see that the ageostrophic contribution on the tracer flux is negligible and the total flux is almost entirely due to the balanced component. On the other hand, for the CW regime shown in Figure 3d, both balanced and ageostrophic components contribute, with the ageostrophic

contribution dominating with increasing wavenumbers or smaller scales. Finally, from Figure 3f revealing the SW tracer flux, we see that $\bar{\hat{\Pi}}_{AG}(k)$ almost entirely determines the total flux $\bar{\hat{\Pi}}(k)$ across all scales and $\bar{\hat{\Pi}}_{G}(k)$ is insignificant. The SW tracer downscale flux is entirely due to ageostrophic flow-induced effects, with negligible contributions from the balanced flow. These observations suggest that ageostrophic motions, that include internal waves, play a substantial role in increasing the downscale transfer of tracer variance and enhancing tracer dispersion. Splitting the horizontal and vertical fluxes also yielded similar results as those shown in the right column of Figure 3 (figures omitted), indicating that ageostrophic flow components have a major say in the lateral and vertical fluxes of tracer variance in the CW and SW regimes.

3.1. Efficiency of the Tracer Cascade

To compare the capabilities of different flows in cascading and dissipating tracer variance, we will now construct the notion of an efficiency associated with the tracer downscale cascade. Multiplying Equation 6 with θ and manipulating the resulting equation gives us an evolution equation for tracer variance in the physical space,

$$\frac{\partial}{\partial t}\left(\frac{\theta^2}{2}\right) + \nabla \cdot \left(\frac{\theta^2 \mathbf{v}}{2}\right) + \frac{\partial}{\partial z}\left(\frac{\theta^2 w}{2}\right) = F_\theta \theta - \gamma \theta^2 - d \tag{12}$$

where $F_\theta\theta$ is the pointwise tracer injection rate, while $d = \nu_\theta \theta \Delta^8 \theta$ represents the pointwise tracer variance dissipation in physical space. If we consider U as an estimate for the flow velocity and L as an estimate for the flow's length scale, the advective terms that succeed the time derivative term in Equation 12, which are responsible for the downscale cascade of the tracer variance, scale as $\theta^2 U/L$.

We now make an important observation. Turbulent fluxes in general fluctuate intermittently in time and space; for example, see detailed discussions on turbulent flow fluxes in Thomas et al. (2024) and Thomas and Ding (2023). The tracer fluxes shown in Figure 3 are a result of time-averaging over a long time interval to remove fast high frequency fluctuations that were seen in individual instances of the flux at different times. The flux can be highly variable and fluctuating in time such that the instantaneous values of the flux are very different from the time-averaged value of the flux. Similarly, spatial distribution of downscale flux can be composed of positive and negative contributions arising from different spatial regions such that the spatially integrated flux is positive (an illustration of this feature in physical space can be seen in the first row of Figure 5 below). As a result, integrated or mean flux estimates are often much lower than the values expected based on scaling estimates. Consequently, the estimate $\theta^2 U/L$ for the nonlinear advective term in Equation 12 is an indication of the fluctuations in the flux and is expected to be higher than the dissipation d, the latter being an estimate for the tracer variance reaching dissipative scales. These observations lead us to define a pointwise efficiency for the tracer downscale cascade as follows:

$$\eta_{\text{pointwise}} \sim \frac{d}{\theta^2 U/L} = \frac{dL}{\theta^2 U}. \tag{13}$$

$\eta_{\text{pointwise}}$ defined above is an estimate for the fraction of fluctuating tracer flux that actually gets dissipated at grid-scale. To get a global estimate rather than a pointwise estimate, we further improve above definition by incorporating volume-integrated quantities that can be computed unambiguously from the numerical solutions. For this we use the scaling relationships

$$D \sim dL^3,\ E \sim U^2 L^3,\ \Theta \sim \theta^2 L^3 \tag{14}$$

where D, E, and Θ refer to domain-integrated tracer dissipation, flow energy, and tracer variance respectively. We then substitute the expressions in Equation 14 into Equation 13 and replace the variables with time-averaged variables to obtain an expression for efficiency of the tracer's downscale cascade as follows:

$$\bar{\eta} = \frac{\bar{D} L^{\frac{5}{2}}}{\bar{\Theta}\ \bar{E}^{\frac{1}{2}}}. \tag{15}$$

We use Equation 15 above to define a global efficiency of the tracer downscale cascade, the efficiency being the ratio of the tracer dissipation to the fluctuations in the tracer flux. As pointed out above, while the advective flux terms fluctuate a lot, only a fraction of it assists the tracer variance in reaching grid scale and dissipating. The tracer cascade efficiency therefore tells us how efficient the stirring and dispersion by the flow is in dissipating tracer variance. We set $L = 2\pi$, the domain length, and computed efficiency for the three flow regimes. The values we obtained were 0.003, 0.06, and 0.08 for the QG, CW, and SW regimes, respectively, and are listed in the final column of Table 1. Interestingly, note that while SW regime showed the highest efficiency, CW regime was 20 times efficient than the QG regime. These estimates indicate that ageostrophic flows are an order of magnitude more efficient than balanced flows in downscale cascading of tracer fields. It is noteworthy that these estimates are similar to the estimates of spectral tracer flux seen in Figure 3: ageostrophic flows have an order of magnitude higher tracer downscale flux than balanced flows.

3.2. Fraction of Linear Waves in the Flow

Above results emphasize that flows with energetic waves are much more efficient in the dispersion of tracers when compared to balanced flow dominant regime. In CW and SW regimes, linear waves were forced at low wavenumbers and we identified the unbalanced flow component as "ageostrophic flow." Nevertheless, these unbalanced flow components could have more than just linear waves. To get a grip on this, we stored all the flow fields at high resolution in time and then performed Fourier transforms in space and time. For example, the horizontal velocity component $u(\mathbf{x}, z, t)$ was used to obtain $\hat{u}(k_h, k_z, \omega)$, and four representative plots are shown in Figure 4. The figure shows $\hat{u}(k_h, k_z, \omega)$ in the $\omega - k_h$ space for different values of k_z in the CW regime. Other flow variables showed similar behavior and is therefore omitted here in the interest of space. The dashed white lines in the figure represent the dispersion relationship given by Equation 5.

In panels (a)–(d) of Figure 4, although we see bright regions that broadly align along the dispersion lines, there is notable spread in the spectra across the dispersion lines. The low wavenumber region, especially in the top row panels, shows some spread towards high frequencies extending well beyond the dispersion lines. This is due to the stochastic forcing we employed to force waves that could produce flat spectrum in the frequency space at and around the forcing wavenumbers. Similar spread can be observed in global ocean models where near-inertial waves and internal tide forcing are implemented (see Muller et al. (2015), for example). However, even away from this low, forcing wavenumber spread, we do see that the flow spectra at higher wavenumbers are spread across the dispersion lines. This indicates that the ageostrophic flow has more than pure linear waves that fall on the dispersion lines. Although the panels (a)–(d) correspond to the CW regime, similar results were seen in the SW regime (figures omitted).

To quantify the linear wave energy content in the flows, we computed the fraction of ageostrophic energy in a small frequency band region ($\delta\omega$) about the dispersion curve. This strategy was adopted by Thomas and Ding (2023) to examine the fraction of linear inertia-gravity waves in a turbulent shallow water system. Qualitatively similar strategies have been used to study turbulent stratified flows (see discussions in Maffioli et al. (2020) and Labarre et al. (2024)). The technique is illustrated in Figure 4e, where the dispersion relationship curve is plotted in red color. Plotting two curves with a distance 0.3 units normal to the dispersion relationship curve on either side gives us the yellow region, this being a region of width $\delta\omega = 0.6$ and contains the dispersion curve. Similarly, the green region in Figure 4e is obtained by plotting curves at a distance 3 units normal to the dispersion relationship curve on either side. By identifying such regions within a certain distance from the dispersion curve, we were able to calculate the flow energy contained in the neighborhood of the dispersion curves in the $\omega - k_h - k_z$ space and we denote this as $E_{\delta\omega}$.

Figure 4f shows the variation of $E_{\delta\omega}/E_{AG}$, that is, the fraction of the ageostrophic energy contained in a region of width $\delta\omega$ around the dispersion curve, as a function of $\delta\omega$. From the figure, we see that for $\delta\omega = 0.6$, which is a region whose boundaries lie really close to the dispersion curve, as seen in panel (e), only about 50% of the ageostrophic energy is associated with this region. Gradually increasing the region width and reaching $\delta\omega = 6$ gives us almost 96% of the ageostrophic energy, although now the region is so wide that its boundaries are far from the dispersion curve as seen in panel (e). These findings were more or less similar in the CW and SW regimes, as seen from the two curves in panel (f), and highlight the fact that although we forced linear internal

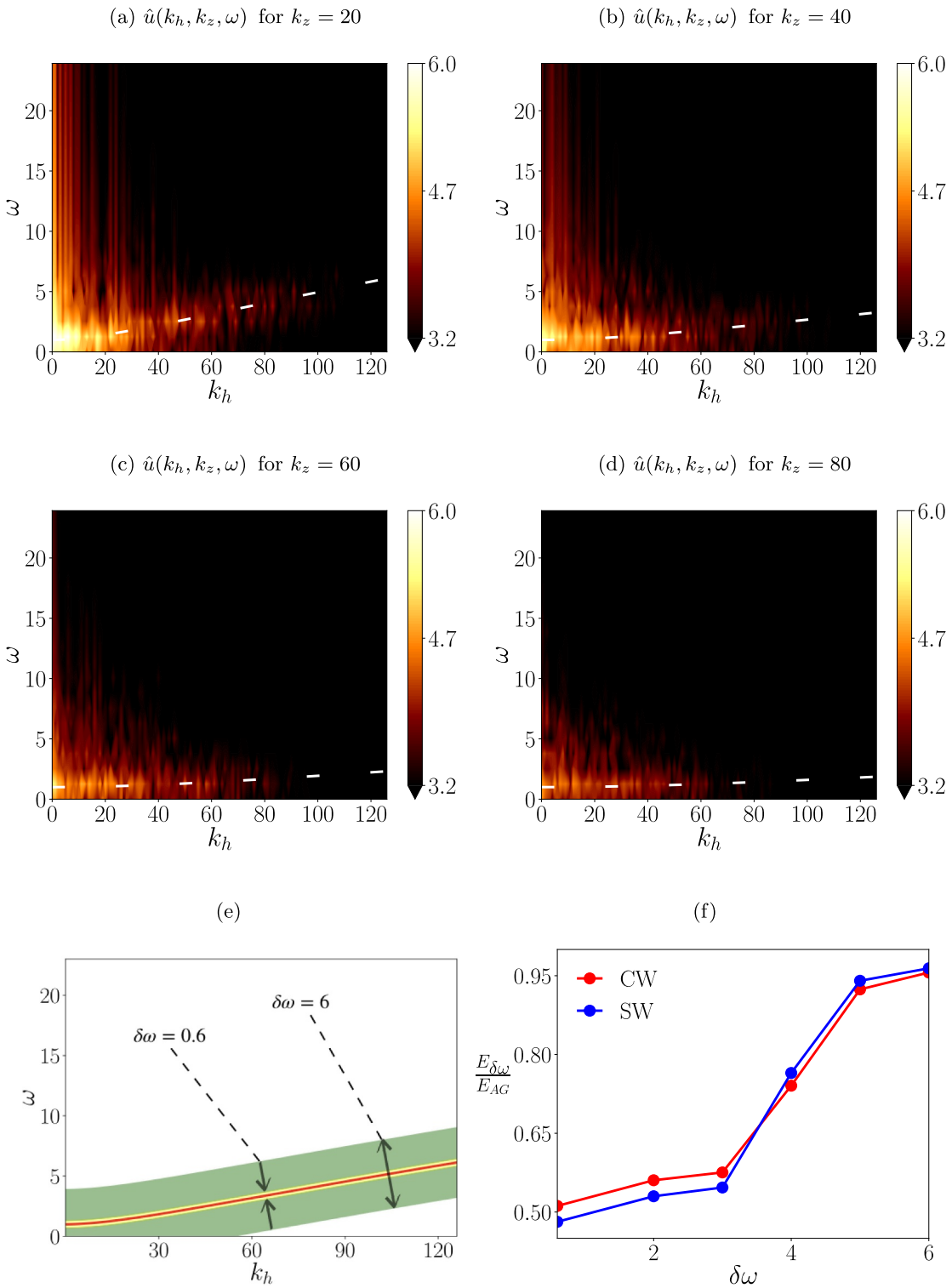

Figure 4. Figure shows $|\hat{u}(k_h, k_z, \omega)|$ for the CW regime on $\omega - k_h$ plane for $k_z = 20$ (a), $k_z = 40$ (b), $k_z = 60$ (c), and $k_z = 80$ (d). Dashed white lines are used to show the dispersion line described by Equation 5. (e) The dispersion line (red color) and regions with different widths around it are shown. (f) Variation of the fraction of the ageostrophic energy contained in the neighborhood of width $\delta\omega$ around the dispersion line.

waves in these two regimes, no more than 50% of the ageostrophic energy can be associated with pure linear waves that follow the dispersion relationship. Rather, the ageostrophic component also contains high frequency components that correspond to a spread in the frequency-wavenumber space. At this point, it is also important to note that since the ageostrophic energy in the SW regime is about double that in the CW regime (recall Table 1), both regimes having about 50% of their energy in linear waves implies that the SW regime has almost double the amount of linear wave energy than the CW regime.

Readers experienced with $\omega - k$ spectra of submesoscale flows will find similarities of frequency-wavenumber spectra shown in Figure 4 with the spectra of previous studies that capture part or whole of the internal wave continuum. For example, Figures 8 and 9 from Ansong et al. (2024) shows horizontal wavenumber-frequency spectra of surface horizontal kinetic energy in different regions of the ocean obtained from MITgcm with a horizontal resolution of $1/24°$ and HYCOM simulations with a resolution of $1/25°$. These figures obtained from the global ocean models also exhibit a spread in the energy across the dispersion line. In Torres et al. (2019), Figures 2a–2c show the $\omega - k_h$ spectra of the sea surface height from a global ocean simulation in the regions Kuroshio Extension, Agulhas Current, and Drake Passage, respectively. Here also we find a spread of energy along the dispersion line similar to our case. Figures 4a and 4b in a more recent work by Yang et al. (2023), which shows frequency-horizontal wavenumber spectrum of internal wave energy at a depth of 33 m from the CROCO model simulations, also exhibit significant spread around dispersion lines.

The results from previous works discussed above indicate notable spread of flow energy beyond the linear internal wave dispersion curve, in some cases much more than what is seen in our low Rossby number spectra shown in Figure 4. Even in our low Rossby number flows, only about 50% of the ageostrophic energy can be associated with pure linear waves. It is therefore important to realize that the ageostrophic energy in turbulent flows containing internal waves can exhibit quite a bit of spread across dispersion lines, and the ageostrophic energy is in general not confined to pure linear waves. This analysis indicate that the tracer stirring and dispersion seen earlier has non-negligible contribution from unbalanced flow components that are not pure linear waves that follow the dispersion relationship.

In the above characterization of waves we used the dispersion relationship as the criterion to identify linear waves. However, it is possible that linear waves that might have existed in the absence of balanced flow or nonlinear interactions got Doppler shifted and moved away from the dispersion curves. One could also think of similar mechanisms transferring flow components that are not linear waves onto the dispersion curves, thereby leading them to be identified as linear waves. While such possibilities are not accounted for in the identification of linear waves, the method is based on a precise definition: we are identifying flow components in the neighborhood of the dispersion curves as linear waves.

Apart from the method we used, there are other flow decomposition techniques adopted in multiple past studies. A fast–slow decomposition applied on the flow components, with a frequency filter identifying frequencies higher than inertial to be "fast" and frequencies lower than inertial to be "slow" is another approach, this being used in Taylor and Straub (2016) and Taylor and Straub (2020). Of course, while this techniques gives us fast and slow components, there is no guarantee that the fast component would be pure linear waves. Instead of relying on the Eulerian flow fields, one could apply the fast-slow decomposition on the Lagrangian flow fields and this has been shown to reduce Doppler shifting effects (see discussions in Nagai et al. (2015); Shakespeare and Hogg (2017, 2018); C. S. Jones et al. (2023)). Once again, while this strategy generates relatively less Doppler-shifted fast component, the component need not be pure linear waves. Consequently, the different flow decomposition methods apply with their own caveats, with no unambiguous and natural choice emerging. In this study, we persisted with the straightforward identification of linear waves based on the dispersion relationship.

3.3. Physical Structure of Tracer Flux

We next look at the tracer flux distribution in physical space. For this we use a low pass filtering operator, $\tilde{\theta} = \mathcal{F}^{-1}\left[\hat{\theta}(k \leq \tilde{k})\right]$, where $\tilde{\theta}$ represents the large-scale tracer field. We apply this filtering operation on Equation 6, ignoring forcing and dissipation, to obtain the following equation:

$$\frac{\partial \tilde{\theta}}{\partial t} + \nabla \cdot \left(\widetilde{\theta \mathbf{v}}\right) + \frac{\partial \left(\widetilde{\theta w}\right)}{\partial z} = 0 \tag{16}$$

Manipulating the above equation further gives us the following equation:

$$\frac{\partial \tilde{\theta}}{\partial t} + \tilde{\mathbf{v}} \cdot \nabla \tilde{\theta} + \tilde{w} \frac{\partial \tilde{\theta}}{\partial z} = \nabla \cdot \left[\widetilde{\mathbf{v}\theta} - \tilde{\mathbf{v}}\tilde{\theta} \right] + \frac{\partial}{\partial z} \left[\widetilde{w\theta} - \tilde{w}\tilde{\theta} \right] \tag{17}$$

Multiplying above equation by $\tilde{\theta}$ and further manipulations give us the following equation:

$$\frac{\partial}{\partial t}\left(\frac{\tilde{\theta}^2}{2}\right) + \frac{1}{2}\left(\nabla \cdot (\tilde{\theta}^2 \tilde{\mathbf{v}}) + \frac{\partial}{\partial z}(\tilde{\theta}^2 \tilde{w}) \right) = \tilde{\theta} \nabla \cdot \left[\widetilde{\mathbf{v}\theta} - \left(\widetilde{\mathbf{v}\theta} \right) \right] + \tilde{\theta} \frac{\partial}{\partial z} \left[\widetilde{w\theta} - \left(\widetilde{w\theta} \right) \right] = -\Pi \tag{18}$$

The first term on the left hand side of Equation 18 is the time rate of change of large-scale tracer variance, $\tilde{\theta}^2/2$, and the second term is the advection of the large-scale tracer variance in the domain, which goes to zero as we integrate Equation 18 throughout the domain. However, the right hand side term $-\Pi$ does not vanish on integrating over the domain and determines the transfer of tracer variance from scales larger than or equal to $1/\tilde{k}$ to smaller scales. We put a negative sign in front of Π since the flux is downscale and therefore the large scales are losing tracer variance to the small scales. Interested readers can refer to chapter 13 of Pope (2000) or chapter 12 of Lesieur (2008) for more details on similar filtering operations.

Figure 5a shows the spatial distribution of Π for the QG regime on the lower half of the domain, with top plane being $z = \pi$ as before, obtained by setting the filter wavenumber $\tilde{k} = 50$. For the following analysis we use the same filter wavenumber, as this scale falls almost in the middle of inertial range and is hence less affected by forcing and dissipation. Other values of $\tilde{k}$ in the inertial range yielded similar results and therefore will not be presented here. It is noteworthy that the flux takes both positive and negative values, as is clear from the histogram of flux shown in Figure 5b. Nevertheless, the mean flux is positive, as seen from the inset figure, indicating a downscale flux. From the histogram and especially from the inset figure, we observe that the mean is more than an order of magnitude smaller than the extreme values of the flux. This feature that is observed in space is generically observed in time as well, that is, turbulent fluxes fluctuate in space and time such that their mean is often much smaller than their extreme values, and we used this insight in constructing the tracer downscale cascading efficiency expression in Equation 15.

We now follow an analysis similar to that in Sirohi and Thomas (2024) to examine the physical space locations that harbor the major share of tracer variance and tracer flux. Given the physical structure of tracer flux, we write the flux at a given time in terms of flow variables, such as geostrophic vorticity and divergence, to obtain $\Pi\left(|\zeta_G|/|\zeta_G|_{\max}\right)$ and $\Pi\left(|\nabla \cdot \mathbf{v}|/|\nabla \cdot \mathbf{v}|_{\max}\right)$, where $|\zeta_G|_{\max}$ and $|\nabla \cdot \mathbf{v}|_{\max}$ are the maximum of the absolute values of geostrophic vorticity and divergence in the domain at that time instant. This representation is numerically achieved by a sorting operation between the flux and the flow variable. For instance, at a particular physical point we identify the normalized geostrophic vorticity value and associate that with the flux at the same point. As a result of this operation, the flux Π becomes a one-dimensional array that depends on other one-dimensional arrays $|\zeta_G|/|\zeta_G|_{\max}$ and $|\nabla \cdot \mathbf{v}|/|\nabla \cdot \mathbf{v}|_{\max}$. We performed the same operation with tracer variance to obtain $\theta^2\left(|\zeta_G|/|\zeta_G|_{\max}\right)$ and $\theta^2\left(|\nabla \cdot \mathbf{v}|/|\nabla \cdot \mathbf{v}|_{\max}\right)$. Having the distribution of tracer flux and tracer variance as a function of flow variables, we computed normalized cumulative sums as follows:

$$\begin{aligned} \Pi_{\zeta_G} &= \frac{\sum_{s=0}^{s=|\zeta_G|/|\zeta_G|_{\max}} \Pi(s)}{\sum_{s=0}^{s=1} \Pi(s)} \quad , \quad \Theta_{\zeta_G} = \frac{\sum_{s=0}^{s=|\zeta_G|/|\zeta_G|_{\max}} \theta^2(s)}{\sum_{s=0}^{s=1} \theta^2(s)} \\ \Pi_{\nabla \cdot \mathbf{v}} &= \frac{\sum_{s=0}^{s=|\nabla \cdot \mathbf{v}|/|\nabla \cdot \mathbf{v}|_{\max}} \Pi(s)}{\sum_{s=0}^{s=1} \Pi(s)} \quad , \quad \Theta_{\nabla \cdot \mathbf{v}} = \frac{\sum_{s=0}^{s=|\nabla \cdot \mathbf{v}|/|\nabla \cdot \mathbf{v}|_{\max}} \theta^2(s)}{\sum_{s=0}^{s=1} \theta^2(s)} \end{aligned} \tag{19}$$

Above, Π_{ζ_G} is the fraction of flux contained in regions with normalized vorticity in the band $\left[0, |\zeta_G|/|\zeta_G|_{\max}\right]$ while $\Pi_{\nabla \cdot \mathbf{v}}$ is the fraction of flux contained in regions with normalized divergence in the band $\left[0, |\nabla \cdot \mathbf{v}|/|\nabla \cdot \mathbf{v}|_{\max}\right]$. Along the same lines, Θ_{ζ_G} and $\Theta_{\nabla \cdot \mathbf{v}}$ are tracer variance fractions contained in similar bands of the flow fields. In the QG regime, dominated by the balanced flow, we computed the flux and tracer variance distributions with respect to ζ_G, while in the SW regime, dominated by internal waves, we computed flux and

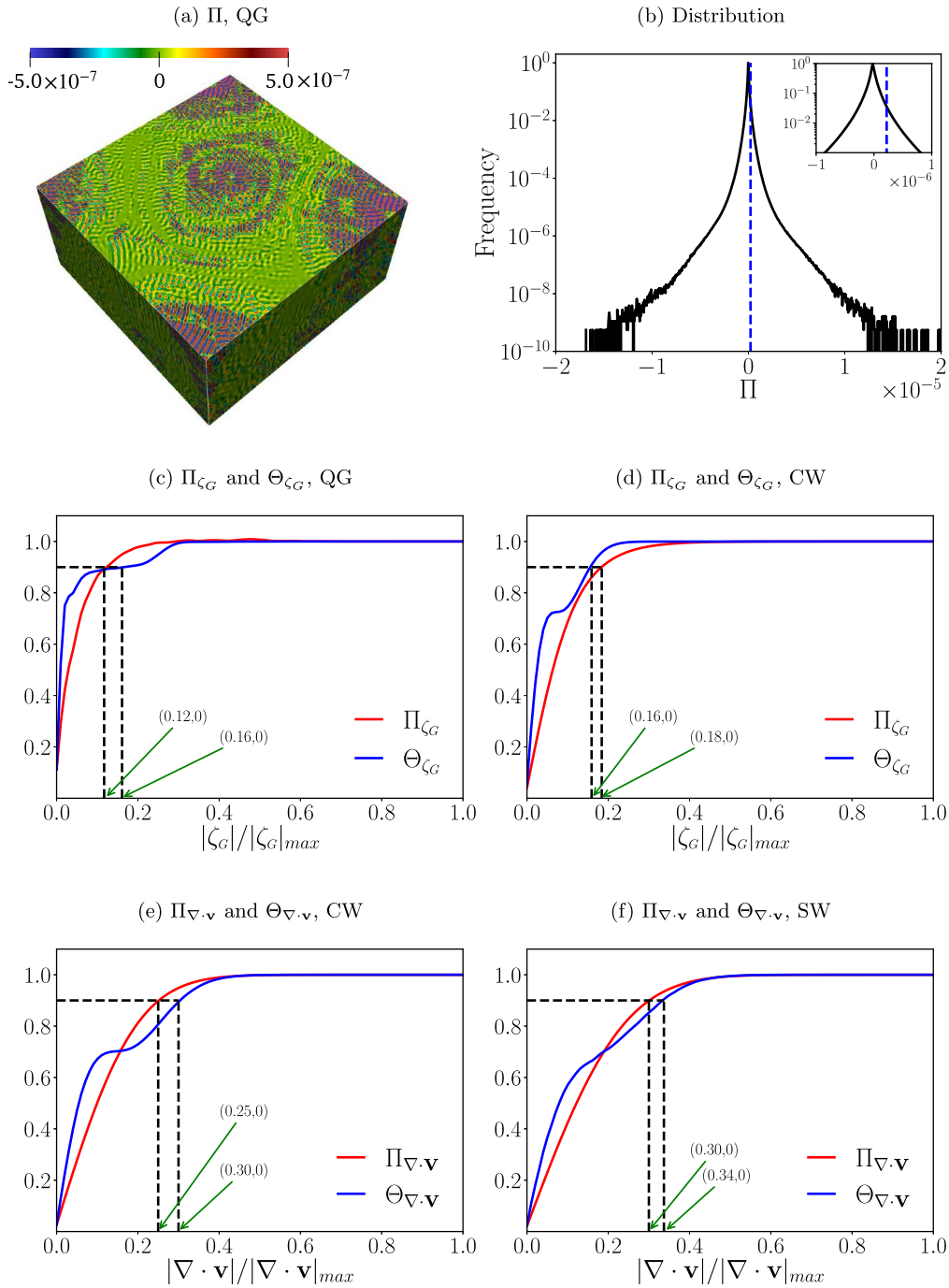

Figure 5. A snapshot of the flux in physical space for the QG regime at an arbitrary time obtained using the low pass filtered Equation 18 is shown in (a), while (b) is the normalized histogram of Π with the blue dashed line being the mean of the distribution. Inset show a zoomed part of the distribution. Cumulative distributions of tracer flux and variance based on expressions given in Equation 19 as a function of ζ_G in QG (panel c) and CW (panel d) and as a function of $\nabla \cdot \mathbf{v}$ in CW (panel e) and SW (panel f) are shown. A rapid increase of the functions to 1 in all the plots indicate that majority of the flux and tracer variance are located in regions with low values of ζ_G and $\nabla \cdot \mathbf{v}$. The $|\zeta_G|/|\zeta_G|_{\max}$ and $|\nabla \cdot \mathbf{v}|/|\nabla \cdot \mathbf{v}|_{\max}$ values at which the functions Π_{ζ_G}, Θ_{ζ_G}, $\Pi_{\nabla \cdot \mathbf{v}}$ and $\Theta_{\nabla \cdot \mathbf{v}}$ reach 0.9 are marked in each of the plots using green arrows for convenient reading of the values.

tracer variance distributions with respect to $\nabla \cdot \mathbf{v}$. Since CW regime has both wave and balanced flow of similar strength, we computed flux and tracer variance distributions with respect to ζ_G and $\nabla \cdot \mathbf{v}$ in this regime. The different variables in Equation 19 were computed and then time-averaged to remove fluctuations in the curves and are then plotted in panels (c)–(f) of Figure 5 for the three flow regimes.

A feature that strikingly stands out in panels (c)–(f) of Figure 5 is the steep and rapid increase of the variables starting at 0 to saturate at 1, suggesting that major share of tracer variance and flux is located in physical space regions where the flow is relatively weak, that is, low values of ζ_G and $\nabla \cdot \mathbf{v}$. For example, from panel (c) (QG regime) we note that 90% of flux and variance is associated with regions where the vorticity magnitude is less than 12% and 16% of the maximum vorticity magnitude. A similar result also holds for the CW regime as seen in panels (d) and (e): 90% of flux and variance is from regions where the vorticity magnitude is less than 16% and 18% of the maximum vorticity magnitude and regions where divergence magnitude is less than around 25% and 30% of the maximum divergence magnitude. For the SW regime shown in panel (f) we see a little more spread in the variables: 90% of flux and variance is from regions where the divergence magnitude is less than 30% and 34% of the divergence magnitude maximum.

Following up on above findings, we will now locate physical space regions that accommodate the major share of flux and variance. For this, in the top row of Figure 6 we have plotted the geostrophic vorticity in the QG regime (panel (a)), CW regime (panel (b)), and the divergence in the SW regime (panel (c)), these being the same physical structures shown in the first column of Figure 1. Now from Figure 5 we see that 0.12 and 0.16 are the normalized geostrophic vorticity values below which the flow fields accommodate 90% of the flux and variance. We used these estimates to plot regions of geostrophic vorticity that contains 90% of the flux and variance in Figures 6d and 6g, respectively, with rest of the regions set to zero and colored in white. As a result of this, Figure 6d shows the geostrophic vorticity field that accommodates 90% of the tracer flux, while Figure 6g shows the geostrophic vorticity field that accommodates 90% of the tracer variance. Similar construction is used to obtain Figures 6e and 6h for the CW regime and Figures 6f and 6i for the SW regime, the last two being divergence plots. Once again we note that the white colored regions are regions excluded or set to zero. Additionally, the top and bottom planes in these figures are $z = \pi$ and $z = 2\pi$, respectively, as in the previous figures.

Comparing the second and third row of Figure 6, we see quite a bit of similarity in the physical space regions that are not white. This observation indicates that the regions that accommodate the major share of the tracer flux are also to a good extent regions that accommodate major share of the tracer variance. Additionally, we see that in the QG and CW regime, coherent vortex cores are excluded white regions. In general, vortex cores are known to act as barriers for the stirring and mixing of tracers, with most of tracer stirring being in strain dominant regions between coherent vortices (see this result discussed in different settings in Shuckburgh and Haynes (2003), Thomas and Gupta (2022), and Sirohi and Thomas (2024)). These previously known findings align with the finding seen in Figure 6, that is, major share of tracer flux being located in regions that exclude vortex cores. For the SW regime, we see that Figures 6f and 6i appear lighter than Figure 6c, as a result of retaining only low divergence regions that accommodate major share of the flux and variance. Since high divergence is associated with regions where wave strengths are high, the results from the last column of Figure 6 reveal that major share of tracer flux and variance is accommodated by weak unbalanced flow energy regions.

Above discussion of the findings from Figures 5 and 6 indicate a common feature of tracer dispersion shared by the three regimes: the major share of tracer flux and variance are accommodated by physical space regions where the flow field is weak, characterized by low values of vorticity and divergence. In some sense this result is unexpected, since any time we see a flow field, our attention immediately turns to high intense flow regions where vorticity and divergence are high. However, the analysis we performed reveal that tracer flux and variance organize themselves in such a way that less intense flow regions can accommodate major share of the flux and variance. Despite the differences exhibited by the three different flow regimes, this aspect appears as a common feature in tracer dispersion dynamics across the three regimes.

We conclude this section by commenting on other relevant flow regimes we examined. As part of this work we did examine flow regimes with wave-balance energy levels different from the three detailed so far and found that the dynamics of those regimes were as expected based on the results from the three regimes discussed in this section. For instance, we found that the regime with energy ratio $E_G/E_{AG} \sim Ro$ had tracer dispersion features that were located between CW and SW regimes; specifically, the tracer spectral flux of this intermediate regime was in between that of CW and SW regimes. Similarly, adding a small amount of wave energy to the QG regime led to

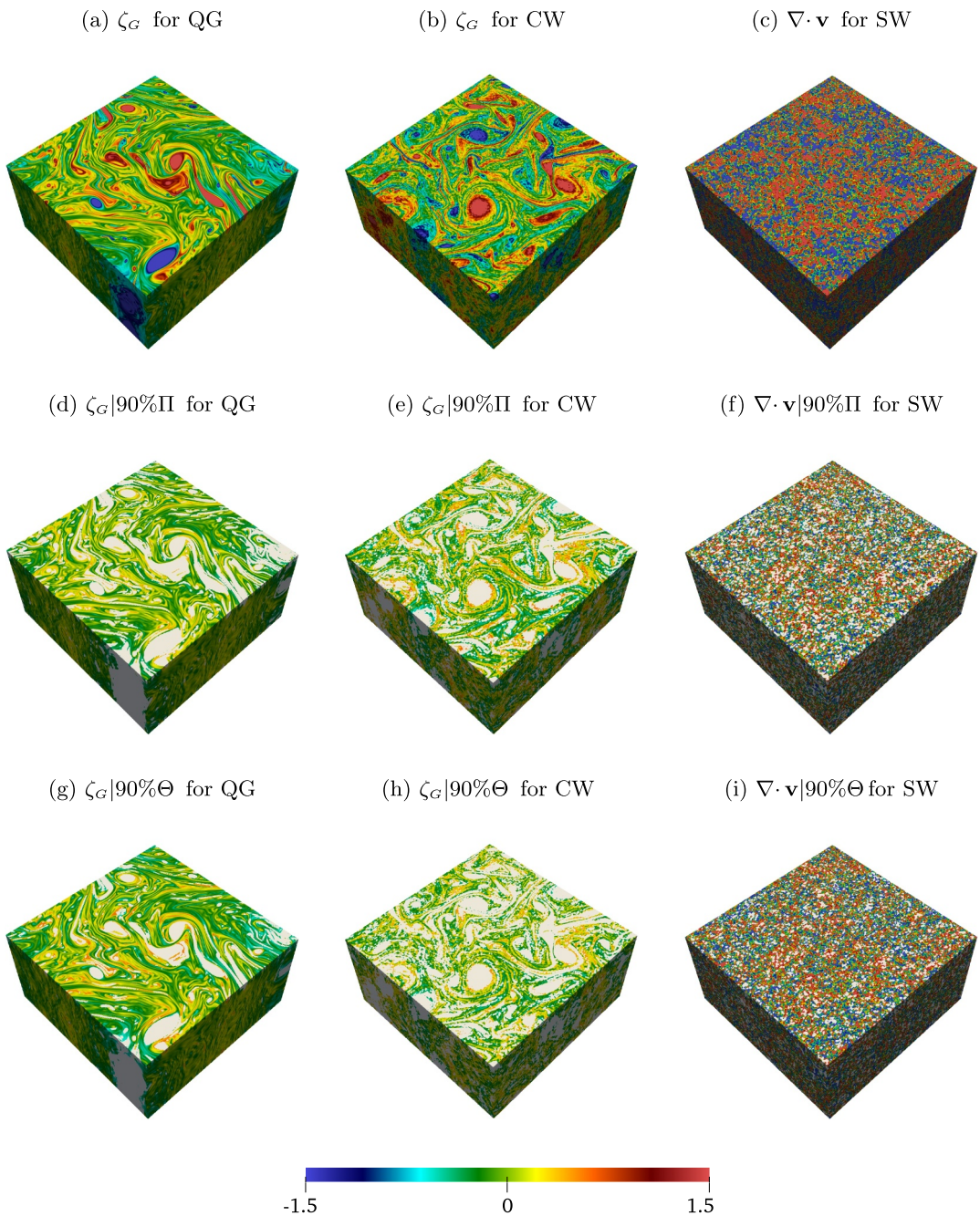

Figure 6. Panels (a) and (b) show ζ_G for QG and CW regimes while panel (c) shows $\nabla\cdot\mathbf{v}$ in SW regime. Panels (d) and (e) show ζ_G at the locations where 90% of flux is accommodated in QG and CW regimes while panel (f) shows $\nabla\cdot\mathbf{v}$ in regions where 90% of flux is accommodated in the SW regime. Panels (g) and (h) show ζ_G in regions where 90% of tracer variance is found in QG and CW regimes while panel (i) shows the $\nabla\cdot\mathbf{v}$ in the regions where 90% of tracer variance is located in the SW regime. The intensity of color is lower in the second and third row compared to the first row, indicating that higher values of the physical fields are zeroed out and whitened.

tracer dispersion features that were slightly increased than that of QG regime. These intermediate regime experiments primarily confirmed to us that the wave-induced enhancement of tracer dispersion monotonically increases as we increase the relative energy of the wave field in the flow.

Finally, we also examined a regime where we initialized and forced only waves. Despite exciting only waves, a small amount of balanced flow was generated due to nonlinear interactions, making this regime close to the SW regime. We did indeed find the tracer dispersion features of this wave-only regime to be almost identical to that of the SW regime. This again could have been anticipated, since as seen from Figure 3f, the balanced flow has almost no contribution to the downscale tracer flux in the SW regime. Consequently, QG and SW regimes may be considered as the extreme cases, with tracer dispersion features of all other regimes with different wave-balance energy ratios expected to be located between the results from these two regimes.

4. Summary and Discussion

Geostrophically balanced mesoscale eddies are ubiquitous in the ocean, carry a major share of the flow kinetic energy, and are considered to be the primary drivers of oceanic tracer dispersion at mesoscales. While the role of balanced eddies in the oceans is well established at large scales, internal gravity waves were conventionally considered to be unbalanced flow components that dominate at much smaller scales and responsible for diapycnal mixing as a result of wave breaking. However, the last two decades of satellite altimeter datasets, in situ measurements, and ocean model outputs have revealed the co-existence of energetic internal waves along with the balanced eddies across different parts of the oceans, with wave energy levels being comparable and sometimes much higher than balanced energy (Lien & Sanford, 2019; Pinkel, 2014; Qiu et al., 2017, 2018, 2022; Richman et al., 2012; Savage & Coauthors, 2017; Tchilibou et al., 2018; Torres et al., 2018; Vladoiu et al., 2024; Yu et al., 2019). These findings have inspired a broad set of wave-balance interaction studies that have described how different kinds of internal waves energetically interact with balanced flow (see discussions and references in Thomas (2023)). Nevertheless, a detailed understanding of the role a broad spectrum of energetic internal waves play in tracer dispersion is still missing, inspiring this study.

In this work we undertook an idealized investigation to study the effect of ageostrophic flows containing internal waves on passive tracer dispersion. We focused in detail on three different flow regimes: QG regime where the flow was almost entirely composed of balanced flow, $E_G/E_{AG} \gg 1$, the CW regime where we forced waves such that the balanced energy was similar in strength to unbalanced flow energy, $E_G/E_{AG} \sim 1$, and the SW regime where unbalanced energy significantly dominated balanced energy, $E_G/E_{AG} \sim Ro^2 \ll 1$, where Ro is the Rossby number. The flows from these three regimes, shown in Figure 1, have very little in common, other than that they all have almost the same total flow energy. The QG regime flow has coherent vortices and have little small scale dissipation, while wave-dominated flows have significant forward energy flux and small-scale dissipation. We generated these idealized flows to examine how the tracer dispersion features change as we go from eddy-dominated to wave-dominated flows. Specifically, we were focused on identifying how finite amplitude or O (1) amplitude waves affect tracer stirring and dispersion, this being a scenario expected in internal wave-rich submesoscale oceanic flows.

To examine dynamics of tracer dispersion in the three flow regimes, we forced and maintained the domain-integrated tracer variance in the three flow regimes. In these experiments we found that the tracer variance spectrum decayed much sharply in the SW and CW regimes with severe depletion of tracer variance in the inertial range when compared to the QG regime, an indication of enhanced stirring and downscale transfer of the tracer field by flows with significant energy in internal waves. On examining the spectral flux of the tracer field, we found that the flux was lowest in the QG regime, increased by an order of magnitude in the CW regime, and was highest in the SW regime. Further splitting the flux based on the contributions from the balanced and unbalanced flow components revealed that the ageostrophic contribution made the difference across the different regimes, with the forward flux of the tracer field increasing monotonically with the increase in the relative energy in the ageostrophic field. We further constructed an efficiency parameter that estimates the ratio of domain-integrated tracer variance dissipation to the advective transport of tracer variance and found that the CW flow was 20 times more efficient than the QG flow, while the SW flow was slightly more efficient than the CW flow. The order of magnitude increase in efficiency with the relative increase in wave energy in the flow was similar to the order of magnitude increase in tracer flux with the relative increase in ageostrophic energy in the flow.

On examining the fraction of linear waves in the flows, we found that despite forcing linear waves at low wavenumbers and being in the small Rossby number regime, only about 50% of the ageostrophic energy could be attributed to linear waves. This was due to the spread of ageostrophic energy across the dispersion curves in the frequency-wavenumber spectra. Consequently, the enhanced stirring of the tracer fields by CW and SW regime

flows had an important contribution from non-wave unbalanced flow components that did not follow the dispersion relationship curves.

We finally examined the physical structure of the tracer flux and its distribution. Interestingly, we found that a major share of the tracer flux was located in physical space regions that were associated with low values of geostrophic vorticity and divergence. Furthermore, these regions where the flux was located also aligned with regions where a major share of the tracer variance was located. Despite the difference in tracer dispersion features of the different flow regimes, this feature was seen to be a common aspect across the regimes: major share of the tracer downscale flux and tracer variance was associated with less intense flow regions.

It is worth noting that the findings from this study corroborate earlier field observations to some extent. The observational study using surface drifters by Meyerjurgens et al. (2020) indicated that baroclinic tides can increase dispersive characteristics of the flow. On a similar note, realistic coastal region simulations by Suanda et al. (2018) showed that dispersion in regions having baroclinic tides is about three to four times higher than regions that lack baroclinic tides. Other noteworthy observational studies have also confirmed that tracer spectra observed in different oceanic regions at submesoscales deviate from the predictions of QG theory. Spiro Jaeger et al. (2020) conducted in situ measurements on spice and observed that an average of all spectra below $\mathcal{O}(10\text{ km})$ scales exhibited a power law slope of approximately k_h^{-2} which is in disagreement with the predictions of QG theory. Klymak et al. (2015) also observed redder spectra at depth which is also in disagreement with QG theory and suggest the possibility of unconsidered depth stirring mechanisms. Similar results are reviewed in Balwada et al. (2024) and the authors comment on internal wave-induced effects potentially modifying tracer dispersion at submesoscales. Based on our findings, we speculate the possibility that internal wave-induced effects could be operating in at least some of the observational studies that find enhanced tracer dispersion at submesoscales.

Despite our attempt to qualitatively compare with observations mentioned above, it is important to note that several realistic ingredients in the ocean were overlooked in the idealized setting we used for this study. This includes bottom topography and boundary layer effects, which can play an important role in oceanic tracer dispersion. Past studies have revealed that bottom topography and other boundary layer effects can break internal waves, which can in turn lead to enhanced mixing of tracers (Gregg et al., 2003; Whalen & Coauthors, 2020). Although our study lacks such realistic boundaries, findings reported here point out that even non-breaking internal waves can have significant role in the lateral dispersion of passive tracers. Furthermore, our findings highlight the importance of parameterizing wave-induced effects in current global ocean models to gain a better understanding of tracer dispersion in oceans, as current models do not fully resolve the internal wave continuum.

Appendix A: Flow and Tracer Forcing

For obtaining the dynamic regimes discussed above, we forced the flow using a stochastic forcing scheme similar to the one discussed in Alvelius (1999). Here we will briefly discuss the forcing scheme. Consider a velocity component, $\hat{u}$, in Fourier space being forced using the forcing $\hat{F}_u$ such that

$$\hat{u}(t+\Delta t) = \hat{u}(t) + \hat{F}_u\,\Delta t \tag{A1}$$

where the dependence of $\hat{u}$ and $\hat{F}_u$ on the wavenumbers k_x, k_y, and k_z is temporarily omitted for convenience. Using above equation, one can write the energy associated with the velocity component in the Fourier space at time $t + \Delta t$ as follows:

$$\frac{1}{2}|\hat{u}(t+\Delta t)|^2 = \frac{1}{2}\left[|\hat{u}(t)|^2 + |\hat{F}_u|^2\Delta t^2 + 2\Delta t\,\mathrm{Re}\left(\hat{F}_u^*\,\hat{u}(t)\right)\right] \tag{A2}$$

where $\mathrm{Re}(g)$ denotes real part of the complex function g. Similarly, one can write equations for other components of the flow v, w, and b using the corresponding forcing components F_v, F_w, and F_b respectively. Adding each of these equations and some rearrangement will give us the following energy equation:

$$\frac{|\hat{E}(t+\Delta t)|-|\hat{E}(t)|}{\Delta t}=\underbrace{\frac{1}{2}\left[\left(|\hat{F}_u|^2+|\hat{F}_v|^2+\frac{|\hat{F}_w|^2}{\alpha^2}+|\hat{F}_b|^2\right)\Delta t\right]}_{\dot{E}_{\mathrm{SD}}}+\underbrace{\left[\mathrm{Re}\left(\hat{F}_u^*\,\hat{u}(t)+\hat{F}_v^*\,\hat{v}(t)+\frac{\hat{F}_w^*\,\hat{w}(t)}{\alpha^2}+\hat{F}_b^*\,\hat{b}(t)\right)\right]}_{\dot{E}_{SID}} \tag{A3}$$

Above α is associated with the vertical velocity contribution to the energy expression, as seen in Equation 2.

In the right hand side of Equation A3, $\dot{E}_{\mathrm{SD}}$ is the sign definite (SD) part while $\dot{E}_{SID}$ is the sign indefinite (*SID*) part. One can chose the forcing terms $\widehat{F}_u$, $\widehat{F}_v$, $\widehat{F}_w$, and $\widehat{F}_b$ such that $\dot{E}_{SID}=0$, making only $\dot{E}_{\mathrm{SD}}$ survive. As a result, $\dot{E}_{\mathrm{SD}}$ becomes the non-negative power input into the system and this balances small-scale dissipation, leading to energy equilibrated flows.

In Section 2 of the manuscript we discussed the flow decomposition into geostrophic and ageostrophic components. As these components are orthogonal in nature, we can write $E=E_G+E_{AG}$. Now, to obtain different flow regimes with desired energy levels, stochastic forcing is applied to each of these components separately. To this end, we can perform similar steps discussed above for the geostrophic and ageostrophic component separately and then arrive at the following equations for the two energy components:

$$\frac{|\hat{E}_G(t+\Delta t)|-|\hat{E}_G(t)|}{\Delta t}=\underbrace{\frac{1}{2}\left[\left(|\hat{F}_{u_G}|^2+|\hat{F}_{v_G}|^2+\frac{|\hat{F}_{w_G}|^2}{\alpha^2}+|\hat{F}_{b_G}|^2\right)\Delta t\right]}_{\dot{E}_{\mathrm{SD}_G}}+\underbrace{\left[\mathrm{Re}\left(\hat{F}_{u_G}^*\,\hat{u}_G(t)+\hat{F}_{v_G}^*\,\hat{v}_G(t)+\frac{\hat{F}_{w_G}^*\,\hat{w}_G(t)}{\alpha^2}+\hat{F}_{b_G}^*\,\hat{b}_G(t)\right)\right]}_{\dot{E}_{SID_G}} \tag{A4a}$$

$$\frac{|\hat{E}_{AG}(t+\Delta t)|-|\hat{E}_{AG}(t)|}{\Delta t}=\underbrace{\frac{1}{2}\left[\left(|\hat{F}_{u_{AG}}|^2+|\hat{F}_{v_{AG}}|^2+\frac{|\hat{F}_{w_{AG}}|^2}{\alpha^2}+|\hat{F}_{b_{AG}}|^2\right)\Delta t\right]}_{\dot{E}_{\mathrm{SD}_{AG}}}+\underbrace{\left[\mathrm{Re}\left(\hat{F}_{u_{AG}}^*\,\hat{u}_{AG}(t)+\hat{F}_{v_{AG}}^*\,\hat{v}_{AG}(t)+\frac{\hat{F}_{w_{AG}}^*\,\hat{w}_{AG}(t)}{\alpha^2}+\hat{F}_{b_{AG}}^*\,\hat{b}_{AG}(t)\right)\right]}_{\dot{E}_{SID_{AG}}} \tag{A4b}$$

At this stage we choose a specific form for $\widehat{F}_{j_G}$ and $\widehat{F}_{j_{AG}}$ as,

$$\widehat{F}_{j_G}=A_G\left(e^{i\phi_{j_G}}+B_G e^{i\phi'_{j_G}}\right) \tag{A5a}$$

$$\widehat{F}_{j_{AG}}=A_{AG}\left(e^{i\phi_{j_{AG}}}+B_{AG} e^{i\phi'_{j_{AG}}}\right) \tag{A5b}$$

where $j\in[u,v,w,b]$, ϕ_{j_G}, $\phi_{j_{AG}}$, ϕ'_{j_G}, and $\phi'_{j_{AG}}$ are random numbers in the interval $[0,2\pi)$ while A_G and A_{AG} are constant real numbers. Using above forms of the forcings and setting $\dot{E}_{SID_G}=\dot{E}_{SID_{AG}}=0$, we obtain B_G and B_{AG} as follows:

$$B_G=-\frac{e^{-i\phi_{u_G}}\,\hat{u}_G+e^{-i\phi_{v_G}}\,\hat{v}_G+e^{-i\phi_{w_G}}\,\hat{w}_G/\alpha^2+e^{-i\phi_{b_G}}\,\hat{b}_G}{e^{-i\phi'_{u_G}}\,\hat{u}_G+e^{-i\phi'_{v_G}}\,\hat{v}_G+e^{-i\phi'_{w_G}}\,\hat{w}_G/\alpha^2+e^{-i\phi'_{b_G}}\,\hat{b}_G} \tag{A6a}$$

$$B_{AG}=-\frac{e^{-i\phi_{u_{AG}}}\,\hat{u}_{AG}+e^{-i\phi_{v_{AG}}}\,\hat{v}_{AG}+e^{-i\phi_{w_{AG}}}\,\hat{w}_{AG}/\alpha^2+e^{-i\phi_{b_{AG}}}\,\hat{b}_{AG}}{e^{-i\phi'_{u_{AG}}}\,\hat{u}_{AG}+e^{-i\phi'_{v_{AG}}}\,\hat{v}_{AG}+e^{-i\phi'_{w_{AG}}}\,\hat{w}_{AG}/\alpha^2+e^{-i\phi'_{b_{AG}}}\,\hat{b}_{AG}} \tag{A6b}$$

Substituting above expressions in Equations A5a and A5b and then using them in A4a and A4b gives us the non-negative power input for the geostrophic and ageostrophic component as $\dot{E}_{\mathrm{SD}_G}$ and $\dot{E}_{\mathrm{SD}_{AG}}$, respectively. Of course, it is possible that the denominators in Equations A6a and A6b can be really close to zero at some specific times and can therefore lead to large values of B_G and B_{AG}. At such times we set $A_G,\ A_{AG} = 0$. Additionally, while time stepping we ensured that the forcing was turned on only when the energy associated with the balanced or unbalanced flow component was reduced by more than 1% of the desired value.

We forced tracers in a different way, by maintaining the tracer variance value at the wavenumber $k = 1$. As discussed earlier, we initialized tracer at $k = 1$, the initial tracer field occupying the entire physical domain. During its temporal evolution, the tracer field gets cascaded to higher wavenumbers and eventually to dissipation scales. To balance the tracer variance loss at large-scales, at each time step we maintained the tracer variance at $k = 1$ as the same initial value, that is,

$$|\hat{\theta}(k=1, t+\Delta t)|^2 = |\hat{\theta}(k=1, t)|^2 + |\delta\hat{\theta}|^2 \tag{A7}$$

where $|\delta\hat{\theta}|^2$ is the amount of tracer variance lost by $k = 1$ mode to other wavenumbers. This forcing acts as a restoring mechanism, replenishing the depleted tracer variance at $k = 1$, the forcing scale.

Appendix B: Two Other Tracer Experiments

Oceanographic in situ experiments aimed at exploring tracer dispersion often release dye tracers in different oceanographic regions and track their evolution with time (J. Ledwell et al., 1993; J. R. Ledwell et al., 1998; M. Sundermeyer & Ledwell, 2001; Shcherbina & Coauthors, 2015). Evaluating the rate at which the tracer variance gets dissipated in these experiments gives an indication of the stirring capacities of the flow. Motivated by these studies, we initialized a tracer field at domain-scale, $k = 1$, and integrated Equation 6 with $F_\theta = \gamma = 0$, that is, no forcing and relaxation terms. To collect an ensemble of results, we initialized the tracer field at low wavenumbers corresponding to domain-scale with random numbers for the Fourier coefficients. Ten different ensembles of initial tracer fields were created and these tracer fields were advected by the QG, CW, and SW regime flows described earlier, resulting in 30 different numerical integrations. For comparing the stirring features of different flows, once a tracer field was initialized randomly, the same tracer field was used in the QG, CW, and SW regimes.

Time evolution of the domain integrated tracer variance $\Theta(t)$, defined in Equation 7, was computed for each of the ensembles after normalizing by the initial values, $\Theta(0)$. Figure B1a shows the ensemble averaged plot of the time evolution of normalized domain integrated tracer variance. We see that the highest rate of decrease in the tracer variance value is seen in the SW regime, followed by the CW regime, and then the QG regime. While in the QG regime only about 50% of initial net tracer variance is lost by final time $t = 250$, the CW and SW regimes lost roughly 80% and 95% of the initial net tracer variance respectively. Comparing the CW and SW regimes, we find that despite the similar drop during the initial times, SW regime exhibit a rapid decrease in later times implying an enhanced dispersion of the tracer variance. The results from the freely evolving tracer experiments point out the relatively weak stirring and mixing capabilities of the balanced flow when compared to the flows that contain internal waves. More specifically, flows having ageostrophic components can cascade tracer fields to smaller scales and dissipate them more efficiently when compared to flows that are dominated by balanced component.

Following the freely evolving tracer experiments described above, we next forced the tracer field at a constant rate with the forcing acting on wavenumbers $k = 1$. Figure B1b shows the time evolution of the normalized domain integrated tracer variance for the three flow regimes. Observe that the QG regime maintains a non-negligible tracer variance in the system, while a steep drop in tracer variance is seen in the CW and SW regimes. The inset in Figure B1b shows that the normalized tracer variance in CW and SW regimes fluctuate around a mean that is about two orders of magnitude lower than in the QG regime. In general, flows that breakdown tracer field into small scales and cascade them downscale at a faster rate will dissipate more tracer variance, leading to their reduction in the domain. Since we injected tracer variance at the same rate for all three flow regimes, the severe reduction of the tracer variance in the CW and SW regimes is an indication of enhanced tracer downscale cascade and small scale dissipation of tracer variance in these two regimes when compared to the QG regime. Consequently, our forced tracer experiments detailed here reveal that flows containing ageostrophic components are

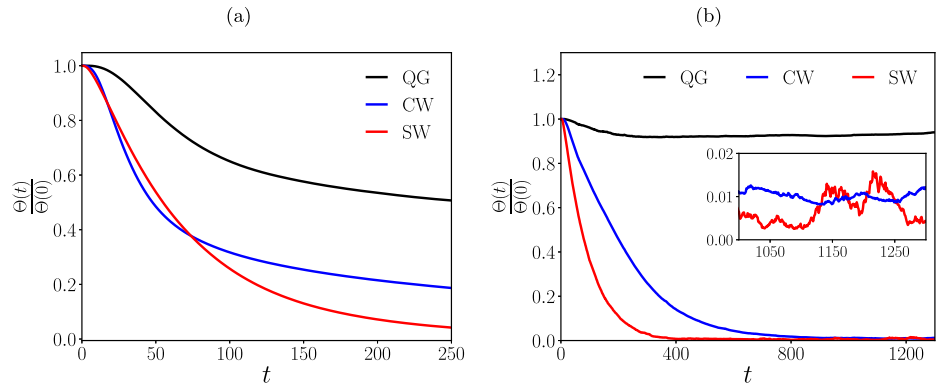

Figure B1. Time series of normalized domain integrated tracer variance, $\Theta(t)$, in the cases of free evolution (a) and constant tracer variance injection rate (b). $\Theta(t)$ is normalized against initial value $\Theta(0)$ for plotting.

more efficient in dispersing tracers when compared to flows that are dominated by the balanced component; this inference is similar to that from the freely evolving experiments described earlier.

Data Availability Statement

The data used for this manuscript and related plotting scripts are available on Zenodo (Sanjay & Thomas, 2025).

Acknowledgments
The authors thank constructive comments and suggestions from reviewers that improved the presentation of results in this paper. Authors also acknowledge discussions that benefited this work from two meetings organized at the International Centre for Theoretical Sciences (ICTS): *Mathematical modeling of Climate, Ocean, and Atmosphere processes* (ICTS/COAPS2023/06) and *Theoretical and Practical Perspectives in Geophysical Fluid Dynamics* (ICTS/TAPGFD2024/05). JT is grateful to the Deep Ocean Mission scheme of the Ministry of Earth Sciences for providing financial support for this work through the project F.No. MoES/PAMC/DOM/18/2022 (E-12926).

References

Alvelius, K. (1999). Random forcing of three-dimensional homogeneous turbulence. *Physics of Fluids*, *11*(7), 1880–1889. https://doi.org/10.1063/1.870050

Ansong, J. K., Arbic, B. K., Nelson, A. D., Alford, M. H., Kunze, E., Menemenlis, D., et al. (2024). Surface and sub-surface kinetic energy wavenumber-frequency spectra in global ocean models and observations. *JGR: Oceans*, *129*(6), e2023JC020480. https://doi.org/10.1029/2023jc020480

Balwada, D., Gray, A. R., Dove, L. A., & Thompson, A. F. (2024). Tracer stirring and variability in the antarctic circumpolar current near the southwest indian ridge. *JGR: Oceans*, *129*(1), e2023JC019811. https://doi.org/10.1029/2023jc019811

Booth, J., & Kamenkovich, I. (2008). Isolating the role of mesoscale eddies in mixing of a passive tracer in an eddy resolving model. *Journal of Geophysical Research: Oceans*, *113*(C5), C05021. https://doi.org/10.1029/2007jc004510

Chouksey, A., Griesel, A., Chouksey, M., & Eden, C. (2022). Changes in global ocean circulation due to isopycnal diffusion. *Journal of Physical Oceanography*, *52*(9), 2219–2235. https://doi.org/10.1175/jpo-d-21-0205.1

Cole, S., & Rudnick, D. (2012). The spatial distribution and annual cycle of upper ocean thermohaline structure. *Journal of Geophysical Research*, *117*(C2), C02027. https://doi.org/10.1029/2011jc007033

Cole, S., Rudnick, D., & Colosi, J. (2010). Seasonal evolution of upper-ocean horizontal structure and the remnant mixed layer. *Journal of Geophysical Research*, *115*(C4), C04012. https://doi.org/10.1029/2009jc005654

Emery, W., Lee, W., & Magaard, L. (1984). Geographic and seasonal distributions of brunt-väisälä frequency and rossby radii in the north pacific and north atlantic. *Journal of Physical Oceanography*, *14*(2), 294–317. https://doi.org/10.1175/1520-0485(1984)014<0294:gasdob>2.0.co;2

Ferrari, R., & Rudnick, D. (2000). Thermohaline variability in the upper ocean. *Journal of Geophysical Research*, *105*(C7), 16857–16884. https://doi.org/10.1029/2000jc900057

Gnanadesikan, A., Bianchi, D., & Pradal, M. (2013). Critical role for mesoscale eddy diffusion in supplying oxygen to hypoxic ocean waters. *Geophysical Research Letters*, *40*(19), 5194–5198. https://doi.org/10.1002/grl.50998

Gnanadesikan, A., Pradal, M. A., & Abernathey, R. (2015). Isopycnal mixing by mesoscale eddies significantly impacts oceanic anthropogenic carbon uptake. *Geophysical Research Letters*, *42*(11), 4249–4255. https://doi.org/10.1002/2015gl064100

Gregg, M. C., Sanford, T. B., & Winkel, D. P. (2003). Reduced mixing from the breaking of internal waves in equatorial waters. *Nature*, *422*(6931), 513–515. https://doi.org/10.1038/nature01507

Hernandez-Duenas, G., Lelong, M.-P., & Smith, L. M. (2021). Impact of wave-vortical interactions on oceanic submesoscale lateral dispersion. *Journal of Physical Oceanography*, *51*(11), 3495–3511. https://doi.org/10.1175/jpo-d-20-0299.1

Holmes, R., Groeskamp, S., Stewart, K., & McDougall, T. (2022). Sensitivity of a coarse-resolution global ocean model to a spatially variable neutral diffusivity. *Journal of Advances in Modeling Earth Systems*, *14*(3), e2021MS002914. https://doi.org/10.1029/2021ms002914

Jones, C., & Abernathey, R. P. (2019). Isopycnal mixing controls deep ocean ventilation. *Geophysical Research Letters*, *46*(22), 13144–13151. https://doi.org/10.1029/2019gl085208

Jones, C. S., Xiao, Q., Abernathey, R. P., & Smith, K. S. (2023). Using lagrangian filtering to remove waves from the ocean surface velocity field. *Journal of Advances in Modeling Earth Systems*, *15*(4), e2022MS003220. https://doi.org/10.1029/2022ms003220

Jones, N., Ivey, G., Rayson, M., & Kelly, S. (2020). Mixing driven by breaking nonlinear internal waves. *Geophysical Research Letters*, *47*(19), e2020GL089591. https://doi.org/10.1029/2020gl089591

Katsumata, K., Talley, L., Capuano, T., & Whalen, C. (2021). Spatial and temporal variability of diapycnal mixing in the indian ocean. *JGR: Oceans*, *126*(7), e2021JC017257. https://doi.org/10.1029/2021jc017257

Klymak, J. M., Crawford, W., Alford, M. H., MacKinnon, J. A., & Pinkel, R. (2015). Along-isopycnal variability of spice in the north pacific. *Journal of Geophysical Research: Oceans*, *120*(3), 2287–2307. https://doi.org/10.1002/2013jc009421

Kunze, E. (2017). Internal-wave-driven mixing: Global geography and budgets. *Journal of Physical Oceanography*, *47*(6), 1325–1345. https://doi.org/10.1175/jpo-d-16-0141.1
Kunze, E., Klymak, J. M., Lien, R. C., Ferrari, R., Lee, M. A., Sundermeyer, C. M., & Goodman, L. (2015). Submesoscale water-mass spectra in the sargasso sea. *Journal of Physical Oceanography*, *45*(5), 1325–1338. https://doi.org/10.1175/jpo-d-14-0108.1
Labarre, V., Augier, P., Krstulovic, G., & Nazarenko, S. (2024). Internal gravity waves in stratified flows with and without vortical modes. *Physical Review Fluids*, *9*(2), 024604. https://doi.org/10.1103/physrevfluids.9.024604
Ledwell, J., Watson, A., & Law, C. (1993). Evidence for slow mixing across the pycnocline from an open-ocean tracer-release experiments. *Nature*, *364*(6439), 701–703. https://doi.org/10.1038/364701a0
Ledwell, J. R., St. Laurent, L. C., Girton, J. B., & Toole, J. M. (2011). Diapycnal mixing in the Antarctic circumpolar current. *Journal of Physical Oceanography*, *41*(1), 241–246. https://doi.org/10.1175/2010JPO4557.1
Ledwell, J. R., Watson, A. J., & Law, C. S. (1998). Mixing of a tracer in the pycnocline. *Journal of Geophysical Research: Oceans*, *103*(C10), 21499–21529. https://doi.org/10.1029/98jc01738
Lesieur, M. (2008). *Turbulence in fluids* (Edition 4). Springer.
Li, G., Cheng, L., Zhu, J., Trenberth, K. E., Mann, M. E., & Abraham, J. P. (2020). Increasing ocean stratification over the past half-century. *Nature Climate Change*, *10*(12), 1116–1123. https://doi.org/10.1038/s41558-020-00918-2
Lien, R.-C., & Sanford, T. B. (2019). Small-scale potential vorticity in the upper ocean thermocline. *Journal of Physical Oceanography*, *49*(7), 1845–1872. https://doi.org/10.1175/jpo-d-18-0052.1
Maffioli, A., Delache, A., & Godeferd, F. S. (2020). Signature and energetics of internal gravity waves in stratified turbulence. *Physical Review Fluids*, *5*(11), 114802. https://doi.org/10.1103/physrevfluids.5.114802
McWilliams, J. C. (2008). The nature and consequences of oceanic eddies. *Geophysical Monograph Series*, *177*, 5–15. https://doi.org/10.1029/177gm03
Meyerjurgens, J., Ricker, M., Schakau, V., Badewien, T. H., & Stanev, E. V. (2020). Relative dispersion of surface drifters in the north sea: The effect of tides on mesoscale diffusivity. *Journal of Geophysical Research: Oceans*, *124*, e2019JC015925. https://doi.org/10.1029/2019JC015925
Muller, M., Arbic, B. K., Richman, J. G., Shriver, J. F., Kunze, E. L., Scott, R. B., et al. (2015). Toward an internal gravity wave spectrum in global ocean models. *Geophysical Research Letters*, *42*(9), 3474–3481. https://doi.org/10.1002/2015gl063365
Nagai, T. A., Tandon, A., Kunze, E., & Mahadevan, A. (2015). Spontaneous generation of near-inertial waves by the kuroshio front. *Journal of Physical Oceanography*, *45*(9), 2381–2406. https://doi.org/10.1175/jpo-d-14-0086.1
Naveira Garabato, A. C., Oliver, K., Watson, A. J., & Messias, M. (2004). Turbulent diapycnal mixing in the nordic seas. *JGR: Oceans*, *109*(C12), C12010. https://doi.org/10.1029/2004jc002411
Pinkel, R. (2014). Vortical and internal wave shear and strain. *Journal of Physical Oceanography*, *44*(8), 2070–2092. https://doi.org/10.1175/jpo-d-13-090.1
Pope, S. B. (2000). *Turbulent flows*. Cambridge University Press.
Qiu, B., Chen, S., Klein, P., Wang, J., Torres, H., Fu, L., & Menemenlis, D. (2018). Seasonality in transition scale from balanced to unbalanced motions in the world ocean. *Journal of Physical Oceanography*, *48*(3), 591–605. https://doi.org/10.1175/jpo-d-17-0169.1
Qiu, B., Nakano, T., Chen, S., & Klein, P. (2017). Submesoscale transition from geostrophic flows to internal waves in the northwestern pacific upper ocean. *Nature Communications*, *8*(1), 14055. https://doi.org/10.1038/ncomms14055
Qiu, B., Nakano, T., Chen, S., & Klein, P. (2022). Bi-directional energy cascades in the pacific ocean from equator to subarctic gyre. *Geophysical Research Letters*, *49*(8), e2022GL097713. https://doi.org/10.1029/2022gl097713
Richman, J. G., Arbic, B. K., Shriver, J. F., Metzger, E. J., & Wallcraft, A. J. (2012). Inferring dynamics from the wavenumber spectra of an eddying global ocean model with embedded tides. *Journal of Geophysical Research*, *117*(C12), C12012. https://doi.org/10.1029/2012jc008364
Sallée, J., Pellichero, V., Akhoudas, C., Pauthenet, E., Vignes, L., Schmidtko, S., et al. (2021). Summertime increases in upper-ocean stratification and mixed-layer depth. *Nature*, *591*(7851), 592–598. https://doi.org/10.1038/s41586-021-03303-x
Sanjay, C. P., & Thomas, J. (2025). Dataset and plotting scripts for 2024JC021754 [Dataset]. *Zenodo*. https://doi.org/10.5281/zenodo.15043512
Savage, A., & Coauthors (2017). Spectral decomposition of internal gravity wave sea surface height in global models. *Journal of Geophysical Research: Oceans*, *122*, 7803–7821. https://doi.org/10.1002/2017JC013009
Shakespeare, C. J., & Hogg, A. M. (2017). Spontaneous surface generation and interior amplification of internal waves in a regional-scale ocean model. *Journal of Physical Oceanography*, *47*(4), 811–826. https://doi.org/10.1175/jpo-d-16-0188.1
Shakespeare, C. J., & Hogg, A. M. (2018). The life cycle of spontaneously generated internal waves. *Journal of Physical Oceanography*, *48*, 343–359. https://doi.org/10.1175/JPO-D-17-0153.1
Shcherbina, A. Y., & Coauthors (2015). The LatMix summer campaign: Submesoscale stirring in the upper ocean. *Bulletin America Meteorology Social*, *96*, 1257–1279. https://doi.org/10.1175/BAMS-D-14-00015.1
Shuckburgh, E. F., & Haynes, P. H. (2003). Diagnosing tracer transport and mixing using a tracer-based coordinate system. *Physics of Fluids*, *15*(11), 3342–3357. https://doi.org/10.1063/1.1610471
Sirohi, M., & Thomas, J. (2024). Passive tracer dispersion by idealized flows across rossby numbers. *Journal of Physical Oceanography*, *54*(9), 1889–1902. https://doi.org/10.1175/jpo-d-23-0132.1
Spiro Jaeger, G., MacKinnon, J. A., Lucas, A. J., Shroyer, E., Nash, J., Tandon, A., et al. (2020). How spice is stirred in the bay of bengal. *Journal of Physical Oceanography*, *50*(9), 2669–2688. https://doi.org/10.1175/jpo-d-19-0077.1
Suanda, S. H., Feddersen, F., Spydell, M. S., & Kumar, N. (2018). The effect of barotropic and baroclinic tides on three-dimensional coastal dispersion. *Geophysical Research Letters*, *45*(20), 11235–11246. https://doi.org/10.1029/2018gl079884
Sundermeyer, M., & Ledwell, J. (2001). Lateral dispersion over the continental shelf: Analysis of dye release experiments. *Journal of Geophysical Research*, *106*(C5), 9603–9621. https://doi.org/10.1029/2000jc900138
Sundermeyer, M. A., & Lelong, M.-P. (2005). Numerical simulations of lateral dispersion by the relaxation of diapycnal mixing events. *Journal of Physical Oceanography*, *35*(12), 2368–2386. https://doi.org/10.1175/jpo2834.1
Taylor, S., & Straub, D. (2016). Forced near-inertial motion and dissipation of low-frequency kinetic energy in a wind-driven channel flow. *Journal of Physical Oceanography*, *46*(1), 79–93. https://doi.org/10.1175/jpo-d-15-0060.1
Taylor, S., & Straub, D. (2020). Effects of adding forced near-inertial motion to a wind-driven channel flow. *Journal of Physical Oceanography*, *50*(10), 2983–2996. https://doi.org/10.1175/jpo-d-19-0299.1
Tchilibou, M., Gourdeau, L., Morrow, R., Serazin, G., Djath, B., & Lyard, F. (2018). Spectral signatures of the tropical pacific dynamics from model and altimetry: A focus on the meso/submesoscale range. *Ocean Science*, *14*(5), 1283–1301. https://doi.org/10.5194/os-14-1283-2018
Thomas, J. (2023). Turbulent wave-balance exchanges in the ocean. *Proceedings of the Royal Society A: Mathematical, Physical and Engineering Sciences*, *479*(2276), 20220565. https://doi.org/10.1098/rspa.2022.0565

Thomas, J., & Daniel, D. (2021). Forward flux and enhanced dissipation of geostrophic balanced energy. *Journal of Fluid Mechanics*, *911*, A60. https://doi.org/10.1017/jfm.2020.1026

Thomas, J., & Ding, L. (2023). Upscale transfer of waves in one-dimensional rotating shallow water. *Journal of Fluid Mechanics*, *961*, A2. https://doi.org/10.1017/jfm.2023.114

Thomas, J., & Gupta, A. (2022). Wave-enhanced tracer dispersion. *Journal of Geophysical Research: Oceans*, *127*(3), e2020JC017005. https://doi.org/10.1029/2020jc017005

Thomas, J., Rajpoot, R. S., & Gupta, P. (2024). The turbulent cascade of inertia-gravity waves in rotating shallow water. *Journal of Fluid Mechanics*, *1000*, A30. https://doi.org/10.1017/jfm.2024.854

Torres, H. S., Klein, P., Menemenlis, D., Qiu, B., Su, Z., Wang, J., et al. (2018). Partitioning ocean motions into balanced motions and internal gravity waves: A modeling study in anticipation of future space missions. *Journal of Geophysical Research: Oceans*, *123*(11), 8084–8105. https://doi.org/10.1029/2018jc014438

Torres, H. S., Klein, P., Siegelman, L., Qiu, B., Chen, S., Ubelmann, C., et al. (2019). Diagnosing ocean-wave-turbulence interactions from space. *Geophysical Research Letters*, *46*(15), 8933–8942. https://doi.org/10.1029/2019gl083675

Vallis, G. K. (2006). *Atmospheric and oceanic fluid dynamics*. Cambridge University Press.

Vladoiu, A., Lien, R., & Kunze, E. (2024). Energy partition between submesoscale internal waves and quasigeostrophic vortical motion in the pycnocline. *Journal of Physical Oceanography*, *54*(6), 1285–1307. https://doi.org/10.1175/jpo-d-23-0090.1

Waterhouse, A., MacKinnon, J. A., Nash, J. D., Alford, M. H., Kunze, E., Simmons, H. L., et al. (2014). Global patterns of diapycnal mixing from measurements of the turbulent dissipation rate. *Journal of Physical Oceanography*, *44*(7), 1854–1872. https://doi.org/10.1175/jpo-d-13-0104.1

Whalen, C. A., de Lavergne, C., Naveira Garabato, A. C., Klymak, J. M., MacKinnon, J. A., & Sheen, K. L. (2020). Internal wave-driven mixing: Governing processes and consequences for climate. *Nature Reviews Earth & Environment*, *1*(11), 606–621. https://doi.org/10.1038/s43017-020-0097-z

Whitwell, C., Jones, N., Ivey, G., Rosevear, M., & Rayson, M. (2024). Ocean mixing in a shelf sea driven by energetic internal waves. *JGR: Oceans*, *129*(2), e2023JC019704. https://doi.org/10.1029/2023jc019704

Yang, L., Barkan, R., Srinivasan, K., McWilliams, J. C., Shakespeare, C. J., & Gibson, A. H. (2023). Oceanic eddies induce a rapid formation of an internal wave continuum. *Communications Earth & Environment*, *4*(1), 484. https://doi.org/10.1038/s43247-023-01137-1

Yu, X., Ponte, S., Elipot, A. L., Menemenlis, D., Zaron, E. D., & Abernathey, R. (2019). Surface kinetic energy distributions in the global oceans from a high-resolution numerical model and surface drifter observations. *Geophysical Research Letters*, *46*(16), 9757–9766. https://doi.org/10.1029/2019gl083074